Journal of Geophysical Research: Oceans

RESEARCH ARTICLE
10.1029/2017JC013539

This article is a companion to Illig et al. [2018], https://doi.org/10.1029/2017JC013540.

Key Points:
- We introduce and validate a simple methodology to estimate gravest CTW mode contributions to coastal variability from ocean model outputs
- Inferred CTW characteristics (modal amplitude and propagating velocities) agree with the solution of a simple multimode linear CTW model
- CTW dynamics controls a large part of the subseasonal variability along the coasts of southwestern American and African continents

Correspondence to:
S. Illig,
serena.illig@ird.fr

Citation:
Illig, S., Cadier, E., Bachèlery, M.-L., & Kersalé, M. (2018). Subseasonal coastal-trapped wave propagations in the southeastern Pacific and Atlantic Oceans: 1. A new approach to estimate wave amplitude. *Journal of Geophysical Research: Oceans*, *123*, 3915–3941. https://doi.org/10.1029/2017JC013539

Received 9 OCT 2017
Accepted 31 MAR 2018
Accepted article online 5 APR 2018
Published online 8 JUN 2018

Subseasonal Coastal-Trapped Wave Propagations in the Southeastern Pacific and Atlantic Oceans: 1. A New Approach to Estimate Wave Amplitude

Serena Illig[1,2], Emeline Cadier[2], Marie-Lou Bachèlery[2,3], and Marion Kersalé[2,4]

[1]Laboratoire d'Etudes en Géophysique et Océanographie Spatiale (LEGOS), CNRS/IRD/UPS/CNES, Toulouse, France, [2]Department of Oceanography, MARE Institute, LMI ICEMASA, University of Cape Town, Cape Town, South Africa, [3]Nansen-Tutu Centre, Marine Research Institute, Department of Oceanography, University of Cape Town, Cape Town, South Africa, [4]NOAA/Atlantic Oceanographic and Meteorological Laboratory, Cooperative Institute for Marine and Atmospheric Studies, University of Miami, Miami, FL, USA

Abstract The Humboldt and the Benguela upwelling systems are connected to the equatorial variability through the coastal waveguide, so that a large variance of the coastal sea level and current variability can be described as an infinite sum of orthonormal free Coastal-Trapped Wave (CTW) modes. The objective of this study is to infer the CTW mode contributions to the coastal variability in both systems at subseasonal timescales (<120 days) from regional ocean circulation model simulations. We develop and validate twin regional model configurations of the southeastern Pacific and Atlantic Oceans. Cross-shore spatial structures of the first four free CTW modes are then derived from model mean stratification and topography along the southwestern African and South American continents. We introduce and validate a new methodology to estimate the gravest CTW mode contributions to model pressure and alongshore current. Our formulation draws on the orthonormality of the CTW modal structures, and uses a simple projection of the coastal and bottom model pressure onto each CTW structure. Results give confidence in the ability of this modal decomposition methodology to disentangle CTW mode contributions from complex nonlinear coastal processes that control the coastal subseasonal variability. In both systems, it allows to successfully extract the gravest poleward propagating CTW modes with velocities close to the theoretical values and amplitudes consistent with the solutions of a simple multimode linear CTW model. Furthermore, results show that both systems exhibit relatively different CTW dynamics and forcings which are discussed in the companion paper (Illig et al., 2018).

Plain Language Summary Coastal-trapped waves propagate in the ocean along the continental shelves, with the coast on their left in the southern hemisphere. They exert an important influence on the coastal circulation and mixing, with notable implications for productive ecosystems. We introduce a new methodology to estimate the amplitude of these waves and their contribution to the coastal sea level and alongshore current variability. It benefits from a relatively simple implementation and is adapted to ocean model solutions. We validate this method using twin regional ocean model configurations of the southeastern Pacific and Atlantic Oceans. This novel approach allows to successfully extract the contribution of the southward propagating coastal waves in these two different systems, with velocities close to the theoretical values and amplitudes consistent with the dynamics of a simple linear coastal model. This gives confidence in the ability of this new technique to disentangle coastal wave contributions from complex nonlinear processes that control the ocean variability in coastal fringes. Furthermore, results show that both systems exhibit drastic differences in the coastal wave dynamics at subseasonal timescales (<120 days) which are discussed in the companion paper (Illig et al., 2018).

1. Introduction

Located in the South-Eastern Pacific (SEP) and South-Eastern Atlantic (SEA) Oceans, the Humboldt and the Benguela upwelling systems host among the most productive ecosystems of the world (Bakun & Weeks, 2008; Chavez et al., 2008). The ocean dynamics is controlled by alongshore equatorward Trade winds. Their

space/time modulation impacts the intensity of the upwelling through Ekman processes (transport and pumping), and forces Coastal-Trapped Waves (CTW). CTW are subinertial waves which propagate along the continental shelves, with the coast on their left in the Southern Hemisphere. These waves can exert an important influence on coastal circulation, exchange, and mixing (Huthnance, 1995). Their periods range from a few days to weeks, with phase speed between $\sim$1 and $\sim$10 m.s^{-1} for different CTW wave modes (Clarke, 1977). Another specific feature of the coastal southeastern Pacific and Atlantic oceans is their relative proximity to the equatorial ocean which makes them particularly sensitive to the oceanic equatorial dynamics (SEP: Belmadani et al., 2012; Brink, 1982; Echevin et al., 2014; Illig et al., 2014; Pizarro et al., 2002; SEA: Bachèlery et al., 2016a, 2016b; Florenchie et al., 2004; Polo et al., 2008; Rouault et al., 2007, 2017). The coastal waveguide can indeed be considered as an extension of the equatorial waveguide, since part of the eastward propagating equatorial wave energy excites poleward-propagating CTW (Clarke, 1983; Enfield et al., 1987; Moore, 1968). Therefore, in the SEA and SEP, two forcings for CTW are at work: the remote equatorial forcing and the local wind stress forcing.

Using sea level data (from altimetry or tide gauges) and current meter measurements, convincing elements have been presented for poleward CTW propagations at subseasonal timescales along the edges of southwestern South American (In situ: Clarke & Ahmed, 1999; Enfield et al., 1987; Hormazabal et al., 2002; Leth, 2000; Pizarro et al., 2001; Shaffer et al., 1997;, Remote: Pizarro et al., 2002) and African (In situ: Schumann & Brink, 1990, Remote: Goubanova et al., 2013; Polo et al., 2008) continents. From the equator down to Northern Angola (12°S), intraseasonal CTW imprint onto the Sea Level Anomalies (SLA) by a few centimeters ($\sim$2 cm) (Polo et al., 2008). Along the West Coast of South Africa, coastal SLA measurement analyses show that wind-stress fluctuations can trigger resonant CTW whose amplitude can peak to 50 cm (Schumann & Brink, 1990). Along the coast of Peru, in the period ranging from days to weeks, SLA and subsurface temperature fluctuations are primarily controlled by remotely forced CTW (Cornejo-Rodriguez & Enfield, 1987; Smith, 1978), mainly during the winter period (Cornejo-Rodriguez & Enfield, 1987). Measurements at 15°S, near Pisco (Peru), also indicate a significant role of wind forcing (Brink et al., 1978; Stuart, 1981). Off Chile, the signature of equatorially forced intraseasonal CTW can be observed as far South as 30°S (Shaffer et al., 1997), where $\sim$15 cm CTW SLA variations have been reported (Leth & Middleton, 2004). At 30°S off Chile, CTW have been shown to amplify the core flow of the Peru-Chile Undercurrent by a factor 3 compared to its mean annual value (Shaffer et al., 1997). In both systems, these results are supported by recent modeling studies in which sensitivity experiments to the remote and local forcings are performed (SEP: Echevin et al., 2014; Illig et al., 2014; SEA: Bachèlery et al., 2016a, 2016b). Along their propagation path, downwelling (upwelling) CTW lead to a deepening (lifting) of the thermocline and the nutricline of the order of tens of meters, and to the poleward (equatorward) advection of shelf waters of up to several hundred kilometers. Furthermore, since primary production can respond to changes in nutrient concentrations on time scales shorter than 50 days, it has been suggested that these waves may have a substantial impact on such very productive ecosystems (Echevin et al., 2014; Shaffer et al., 1997).

The formalism of CTW is well established for free inviscid CTW (Brink, 1989, 1991; Huthnance, 1978). Where the long wave assumption (frequencies smaller than the inertial frequency and alongshore scales of motion larger than the shelf width) can be satisfied, CTW can be represented by a sum of gravest modes whose spatial structure and phase velocity depend on cross-shore topography and stratification (Brink & Chapman, 1987). The amplitude of these modes satisfies a fully coupled infinite set of forced, first-order wave equations (Clarke & Brink, 1985), in which the CTW amplitude is controlled by the equatorial forcing, the alongshore wind-stress fluctuations, the frictional dissipation, and the modal energy scattering.

Using in situ measurements several approaches have been developed to estimate the amplitude of CTW. From sparse in situ observations, Church et al. (1986a) inferred the amplitude of CTW modes from measurements taken from mooring lines. These authors describe the observed coastal variability as a linear combination of the three gravest CTW modes and an empirical eddy mode. CTW amplitudes that satisfy this set of equations minimizing the residual by least squares fitting are the Moore-Penrose solution. However, this procedure needs a large data set, which samples the water column where the CTW spatial structures are orthogonal. On the other hand, Clarke and Van Gorder (1986) presented a practical method for solving the CTW coupled set of equations. They provided the formulation of a simple multimode linear model in which CTW travel only in one direction along the coastline and are subject to a boundary condition at the starting point, i.e., the equatorial forcing in the SEP and SEA coastal systems. These formalisms were remarkably

successful in predicting coastal observed sea level and alongshore current time series in many different regions including Australia (Church et al., 1986a, 1986b), the Mediterranean Sea (Jordi et al., 2005), the East China Sea (Yin et al., 2014), the West Florida shelf (Mitchum & Clarke, 1986), as well as in the California (Chapman, 1987, Davis & Bogden, 1989) and Humboldt (Brink, 1982; Pizarro et al., 2001) current systems.

Despite the important contribution of CTW to the coastal dynamics in both sectors, a limited amount of research has been made to describe CTW characteristics along the southwestern African continent. Also, to our knowledge, there are no previous studies confirming that observed CTW in the SEA have modal structures and propagation characteristics consistent with the one expected from the theoretical background. The objective of this study is to provide useful materials for the identification, and the estimation of CTW mode contribution to coastal variability in the two systems, in order to explain their similarities and differences at subseasonal timescales as observed from altimetry (cf., the companion paper, Illig et al., 2018). Due to the lack of an adequate observation network in the two regions of interest, our approach is based on numerical experimentation with a regional ocean circulation model, with the objective of estimating free CTW modal structures, amplitudes and parameters (namely their phase speed, frictional and wind projection coefficients) along the southwestern South American and African coasts. We will explore a new approach for estimating the amplitude of the gravest CTW modes based on the orthonormality property (Brink, 1989; Clarke, 1977) of the CTW modal structures along the coast. This methodology is relatively simple to implement and is adapted to model solutions where bottom pressure values are available. The skills of this methodology will be evaluated in the light of the solutions of a simple multimode CTW linear model. We will take advantage of the differences between the two systems that will provide various configurations to test out our modal decomposition methodology. We will also discuss the CTW contributions obtained from the existing semiempirical methodology developed by Church et al. (1986a). Notably, the estimation of free CTW parameters and CTW amplitudes from model mean stratification and cross-shore topography is a prerequisite before inferring and comparing the characteristics of each CTW mode along the coastal American and African systems. Our results will also allow disentangling the signature of CTW propagations triggered by local wind-stress fluctuations on the coastal variability from the one associated with the remote equatorial forcing. This will be the objective of the companion paper (Illig et al., 2018).

The paper is structured as follows: observed data sets and global reanalysis used in this study are described in section 2. Section 3 introduces the twin regional ocean circulation model configurations of the southeastern Pacific and Atlantic Oceans and their validation against in situ and satellite data. Section 4 is devoted to a brief review of the CTW theory, the description of the methodologies used to estimate the amplitude of the gravest CTW modes, and the formulation of the simple multimode CTW linear model. In section 5, derived gravest CTW mode contributions to the coastal subseasonal variability obtained with our new methodology are compared to linear CTW model solutions and CTW characteristics are evaluated against the theoretical background. Section 6 provides a discussion of our results and an analysis of sensitivity experiments carried out with the methodology developed by Church et al. (1986a), followed by concluding remarks and perspectives to this work.

2. Data and Methods

For the forcing and the estimation of our regional model performances, in situ and remote sensing data, along with reanalysis outputs are used.

2.1. Satellite Data

Wind and Wind-Stress: The near-surface atmospheric circulation over the ocean is described using daily zonal and meridional wind stress components from the NASA satellite QuikSCAT (Blanke et al., 2005). Homogeneous temporal series of daily mean wind and wind stress fields, on global $0.5° \times 0.5°$ resolution grids, are generated from L2B product (distributed by JPL/PO.DAAC) by the French ERS Processing and Archiving Facility CERSAT (http://cersat.ifremer.fr/data/products/catalogue). Note that in the near-coastal region, QuikSCAT wind stress data are masked and are not available within ~25 km off the coast due to land contamination. For modeling purposes, an extrapolation of wind amplitude and momentum fluxes was performed within QuikSCAT blind zone using a simple near-neighbor procedure.

SLA: We use the gridded AVISO combined product for SLA, provided by the Ocean Topography EXperiment TOPEX/Poseidon/Jason and the European Remote Sensing Satellite ERS-1/2 data sets, from January 2000 up to December 2008 with a weekly frequency on a 1/3° Mercator grid (Ducet et al., 2000; Le Traon et al., 1998). Data can be downloaded from Aviso+ data server (http://www.aviso.altimetry.fr/en/data/products).

2.2. Global Reanalysis

Oceanic Reanalysis: 5 day averages of the Simple Ocean Data Assimilation (SODA) outputs mapped onto a uniform 0.5° × 0.5° × 40 level grid (19 vertical levels in the upper 500 m depth) are prescribed as initial and open lateral boundary conditions for our regional ocean model simulations (cf., section 3.1). SODA combines the Los Alamos implementation of the POP (Parallel Ocean Program) model with a sequential estimation data assimilation method (Carton et al., 2000; Carton & Giese, 2008). The version used for this paper (SODA 2.1.6) is forced by outputs from the European ReAnalysis-40 (ERA-40) from 1958 to 2001 and then by ERA-Interim for the period spanning from 2002 to 2008. SODA 2.1.6 assimilates all available data from hydrographic stations, expendable bathythermographs, and floats, but does not use satellite altimetry. In this version, hydrographic observations come from WOD09 (Boyer et al., 2009) using their standard level temperature and salinity data. More details of the SODA system can be found in Carton et al. (2005) and in Carton and Giese (2008). Data can be downloaded from the SODA/TAMU data server (http://soda.tamu.edu/data.htm).

Atmospheric Reanalysis: For consistency with the use of SODA, we used daily averages of ocean surface heat and water forcings (2 m air temperature and humidity, shortwave, long-wave, and precipitations) from the European Center for Medium-Range Weather (ECMWF) ERA-Interim reanalysis (Dee et al., 2011) for our ocean simulations. ERA-Interim data sets are available from 1979 to present on a T255 horizontal resolution with 60 vertical levels. Data can be downloaded from the ECMWF data server (http://apps.ecmwf.int/datasets/data/interim-full-daily).

2.3. Estimation of the Remote Equatorial Forcing

SODA 2.1.6 model outputs are further used to quantify the equatorial forcing over the 2000–2008 period. Note that the coarse temporal resolution of SODA forcing at our disposal (5 day) prevents the analysis of periods lower than 10 days, and in particular the role of mixed Rossby gravity waves (Enfield et al., 1987) will not be addressed in this study.

Equatorial Kelvin Wave (EKW) amplitudes are estimated using a modal decomposition of the variability (pressure and zonal current). SODA outputs have shown to be efficient in capturing the salient features of the propagating characteristics (phase speed and amplitude) of EKW contributions for both the equatorial Pacific (Dewitte et al., 2008a, 2008b; Illig et al., 2014) and Atlantic (Bachèlery et al., 2016a; Goubanova et al., 2013) Oceans. Contributions of the first four EKW modes in the Pacific and the Atlantic Oceans are computed following the methodology described in Illig et al. (2004). This method consists in deriving vertical modes from seasonally and zonally slow-varying stratification over which pressure and zonal current anomalies are projected. This provides the baroclinic mode contributions to sea level and zonal current which are then projected onto the theoretical meridional structures of EKW, accounting explicitly for the coastal boundary near the equator in the Gulf of Guinea (Cane & Sarachik, 1979). EKW are expressed in terms of the amplitude of EKW contribution to sea level anomalies.

2.4. Climatology and Subseasonal Anomalies

Data and model monthly climatologies are estimated over the 2000–2008 period. They are then interpolated onto a daily time axis using cubic splines.

In order to isolate the subseasonal variability, we use the methodology from Goubanova et al. (2013), Illig et al. (2014), and Bachèlery et al. (2016a). Subseasonal anomalies are estimated as the departure from the 1–2-1 monthly running weighted average time series. In order to ensure that no seasonal cycle remains, the monthly climatology is also removed. This method is similar to a high-pass filter with a transfer function characterized by a −1, −3, −10 dB attenuation (79%, 50%, 10% of the input power survives) at 117, 168, 466 day, respectively (Mosquera-Vásquez et al., 2014).

3. Regional Oceanic Simulations

In order to estimate the CTW subseasonal contribution along the coasts of Peru/Chili and Southwest Africa, we developed twin regional oceanic model configurations of the southeastern Pacific and Atlantic Oceans. This section is devoted to the description of these configurations, followed by a brief analysis of the model performances with regards to the mean state and the subseasonal variability.

3.1. Regional Ocean Model Configurations

Regional oceanic simulations were performed with the AGRIF version (Debreu et al., 2012; Penven et al., 2006) of the Regional Ocean Modeling System (ROMS, Shchepetkin & McWilliams, 2005) version 3.1 available at www.romsagrif.org. ROMS is a split explicit, free-surface, topography-following coordinate model that solves the three-dimensional Reynolds-averaged Navier-Stokes equations based on the Boussinesq and hydrostatic approximations. ROMS uses finite-difference approximations on a horizontal curvilinear Arakawa C grid and on a vertical stretched terrain-following coordinate system. Momentum, scalar advection, and diffusive processes are solved using transport equations. An equation of state computes the density field that accounts for temperature and salinity. A third-order upstream biased advection scheme (Shchepetkin & McWilliams, 1998) is used for momentum and tracers, while the subgrid-scale vertical mixing is parameterized using a K-Profile Parameterization (KPP) boundary layer scheme (Large et al., 1994). Explicit lateral viscosity is null everywhere in the model, except in sponge layers near the open boundaries.

Our southeastern Pacific ROMS configuration ($ROMS_{SEP}$) resembles the one of Dewitte et al. (2012). The domain covers the region between 40°S and 12°N, spanning from 95°W to the South American coast (Figure 1c). The southeastern Atlantic configuration ($ROMS_{SEA}$) is similar to the one developed in Bachèlery et al. (2016a), extending from 30°S to 7°N and from 10°W to the southwestern coast of the African continent (Figure 1d). Both configurations are developed at an eddy-resolving resolution of 1/12°, with 37 sigma vertical levels stretched in the surface layer. Within the SEP (SEA), configuration model North/West/South (West/South) lateral boundaries are open using a mixed radiation-nudging scheme (Marchesiello et al., 2001), and forced by 5 day mean temperature, salinity, sea level, and currents fields derived from SODA reanalysis (see section 2.3). Initial conditions (potential temperature, salinity, horizontal current, and sea surface height) are estimated from January 2000 SODA outputs. Topography is derived from GEBCO_08 global elevation database at 30 arc-second spatial resolution (http://www.gebco.net). Note also that a linear adjustment of ROMS model bathymetry to SODA bathymetry is made at ROMS open lateral boundaries within a 2° width band in order to ensure continuity of both model solutions (SODA and ROMS). The 10 m-wind amplitude and wind stress forcings come from daily QuikSCAT gridded data, while for surface heat/water flux forcing, we used daily averages of atmospheric ERA-Interim reanalysis using bulk formulations (Kondo, 1975). As no river discharges are taken into account in $ROMS_{SEA}$ simulations, model Sea Surface Salinity (SSS) is restored to the 5 day-interannual SODA SSS.

For both configurations, model solutions reached a statistical equilibrium (in terms of upper ocean stratification and eddy kinetic energy levels) after 5 years of spin-up performed by forcing the model with climatological forcings estimated over the 2000–2008 period. Then, simulations were performed over the 9 years spanning the 2000–2008 period, during which daily averages of model state variables (temperature, salinity, currents, and sea surface height) were stored. The pressure field is calculated offline as the integral of the density from the sea level to the bottom of the ocean, using the Thermodynamic Equation Of SeaWater 2010 (TEOS-10) from Gibbs-SeaWater Oceanographic Toolbox (McDougall & Barker, 2011).

3.2. Evaluation of Model Performances

In this section, we evaluate the realism of our ROMS regional simulations in the SEP and SEA sectors over the 2000–2008 period. Note that similar simulations have been validated in Dewitte et al. (2012), Illig et al. (2014), and Bachèlery et al. (2016a). We focus here on the validation of the key properties that control CTW characteristics, namely; (i) the mean vertical structure along the coast which shapes the CTW mode structures (see section 4) and (ii) the subseasonal variability which determines the subseasonal CTW mode contributions (timescale of interest in this study).

The mean vertical stratification is well reproduced by our ROMS configurations. This is illustrated by the reasonable cross-shore sections along the Peruvian (Figure 1a, averaged within (8°S–13°S)) and the Namibian

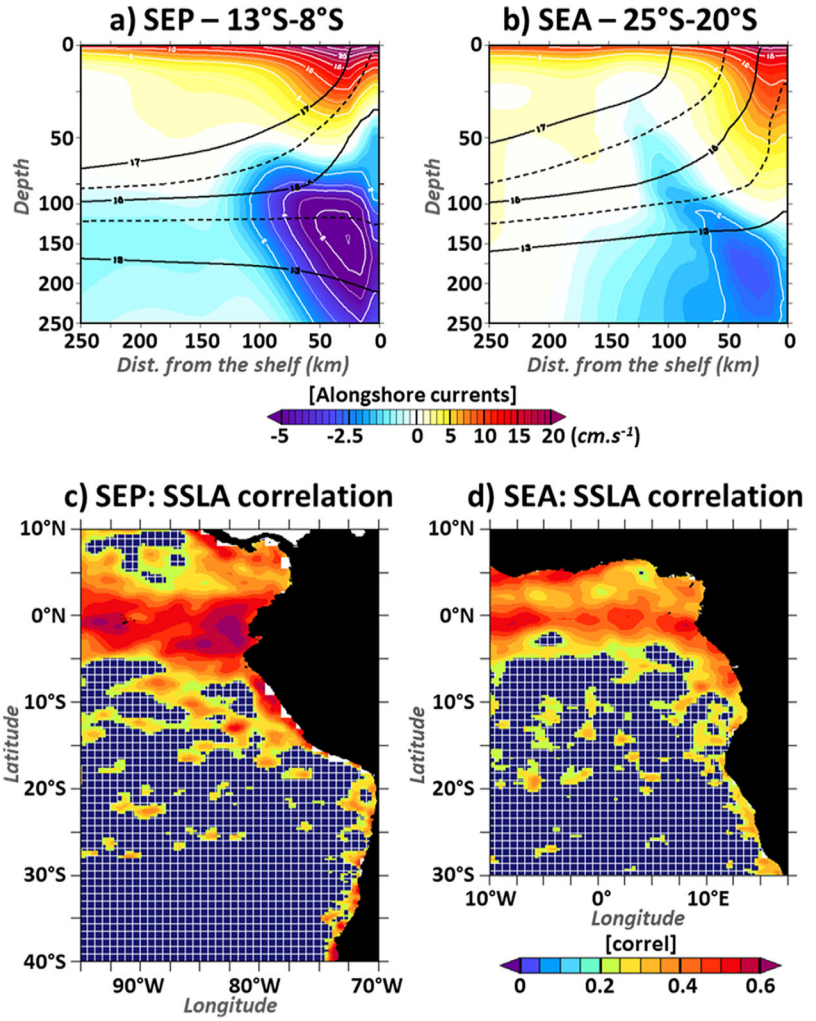

Figure 1. ROMS performance over the 2000–2008 period: (top) mean vertical cross-shore sections averaged along the Peruvian coast between 8°S and 13°S (a) and along the Namibian coast between 20°S and 25°S (b) in function of depth (m) and distance from the shelf (km). Alongshore currents (cm s^{-1}) are in color and white contours. 13–15–17°C and 14–16°C mean isotherms are displayed in plain and dashed black lines, respectively. (bottom) Correlation maps between modeled and observed (AVISO) 7 day averaged Subseasonal Sea Level Anomalies (SSLA) over (c) the South-Eastern Pacific (SEP) and (d) the South-Eastern Atlantic (SEA) sectors. Blue square patterns denote nonsignificant correlations (95% confidence threshold, Sciremammano, 1979).

coasts (Figure 1b, averaged within (20°S–25°S)). The coastal upwelling signature is clearly marked in the model outputs, as depicted by the coastward shoaling of the isotherms within 100 km from the coast, in agreement with observational sections reported in the literature (Illig et al., 2014, Figure 2 and Gutknecht et al., 2013, Figure 5). The differences between CARS2009 (Dunn & Ridgway, 2002; Ridgway et al., 2002) and ROMS temperatures along these sections do not exceed 2°C within the thermocline (not shown). The mean SST is also realistic, with a noticeable cool bias (∼1.5°C) in the coastal regions, which can be attributed to the use of extrapolated QuikSCAT data in the coastal blind zone that tends to overestimate coastal wind and associated upwelling (Desbiolles et al., 2016). The alongshore circulation in these eastern boundary upwelling systems is well reproduced; portraying surface geostrophic equatorward currents and poleward well-defined undercurrents, in agreement with the modeling results of Dewitte et al. (2012) (their Figure 3) and Bachèlery (2016) (her Figure 2.5). This realism of the vertical current structure and the associated shear shape ROMS SEP and SEA mean geostrophic Eddy Kinetic Energy (EKE) patterns (not shown) which are coherent with altimetry estimations, in agreement to analogous SEP (Dewitte et al., 2012) and SEA

(Bachèlery et al., 2016a) ROMS configurations at 1/12° resolution. To assess the model skills in reproducing the subseasonal variability, weekly averaged ROMS Subseasonal Sea level Anomalies (SSLA) are compared to altimetric data (AVISO) in both sectors (SEP Figure 1c and SEA Figure 1d). Correlations between model and observations are statistically significant, with values larger than 0.5, along the equatorial waveguides and along the southwest coast of the neighboring continents. This highlights the realistic subseasonal variability in the coastal fringe associated with remotely forced CTW and locally forced processes such as CTW and upwelling variability. Note that further offshore, the lack of agreement between model and observations can be attributed to the mesoscale activity: in absence of data assimilation, observed and simulated eddies are not expected to agree in their individual features.

In conclusion, the a priori low resolution (∼8 km) of the model configurations to solve the boundary layer dynamics compared to the ∼5 km upwelling scales (Marchesiello & Estrade, 2010) is not detrimental for achieving a fair realism of the parameters relevant for this study. The realism of our twin configurations of the SEP and the SEA gives confidence to further estimate the characteristics of the subseasonal CTW propagations in these two systems.

4. Coastal-Trapped Wave Decomposition

For the sake of completeness, we summarize in this section the CTW theory. It is followed by the description of the methodologies developed to extract the subseasonal CTW contribution to ROMS coastal variability and the formulation of a linear CTW model.

4.1. Coastal-Trapped Waves Theory

Considering a linear Boussinesq, hydrostatic, free-surface ocean with frequencies smaller than the inertial frequency f, and with alongshore scales larger than the cross-shelf scales, the equation of motion can be solved by expanding the pressure perturbation p as free CTW modal structures F_n and their associated amplitude ϕ_n (Brink, 1982; Chapman, 1987; Clarke & Van Gorder, 1986), such as:

$$p(x,y,z,t)=\sum_{n=1}^{+\infty} F_n(x,z)\phi_n(y,t) \tag{1}$$

where x, y and z are cross-shelf (positive offshore), alongshore (positive poleward), and vertical (positive upward) coordinates, and t is the time. For a slow varying medium, the eigenfunctions $F_n(x,z)$ represents the free-wave modal structures which vary in the cross-shelf and vertical directions. They are solution to the following eigenvalue problem:

$$(F_n)_{xx}+f^2\left(\frac{(F_n)_z}{N^2}\right)_z=0 \tag{2a}$$

subject to boundary conditions:

(2b) Free surface: $g(F_n)_z+N^2F_n=0$ at $z=0$

(2c) No flow through the bottom: $(F_n)_z+N^2h_xf^{-2}\left[(F_n)_x+fc_n^{-1}F_n\right]=0$ at $z=-h(x)$

(2d) No flow through the coast: $(F_n)_x+fc_n^{-1}F_n=0$ at $x=0$

(2e) Coastal trapping: $F_n\rightarrow 0$ at $x\rightarrow\infty$

where $N^2(z)$ is the buoyancy frequency and $h(x)$ is the water depth which increases monotonically offshore until reaching a constant depth (see schematics on Figure 2b). f is the Coriolis parameter and subscripts x and z represent partial differentiation. The free-wave phase speed (c_n) is the eigenvalue of this problem.

Modal structures are orthonormal according to energy conservation (Brink, 1989), such as:

$$F_n\otimes F_m=f^{-1}\left(\int_{-h(0)}^{0}[F_nF_m]_{x=0}\,dz+\int_0^{\infty}h_x[F_nF_m]_{z=-h}\,dx\right)=\delta_{nm} \tag{3}$$

where δ_{nm} is the Kronecker delta. Only values of the eigenfunctions on the sloping shelf and coast are relevant, and it is where the eigenfunctions form a complete set.

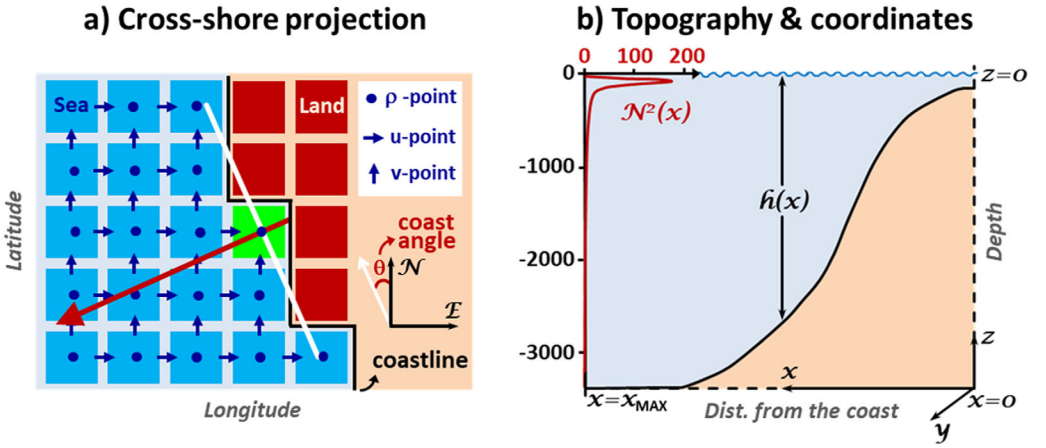

Figure 2. (a) ROMS-staggered Arakawa C-grid schematic with coastline positioned between land (red squares) and sea (blue squares) cells. For each latitude, coast angle (θ) and alongshore direction (white line) are determined by estimating the least-squares best-fit straight line over a 2°-centered latitudinal width coastline position array. Cross-shore sections (red arrow), perpendicular to the alongshore directions, pass through the rho-grid points closest to the coast (green square). At each longitude and vertical levels, we interpolate ROMS fields onto the cross-shore paths using a bilinear interpolation scheme. Model pressure and bathymetry at the coast (x = 0) are extrapolated from the near-shore rho-grid point. (b) Cross-shore coordinate system definition, with cross-shore topography profile (h(x)) and offshore Brunt-Väisälä frequency ($N^2(x = x_{MAX})$, in 10^{-6} $rad^2.s^{-2}$). Note that, in order to be able to average ROMS fields in time (with time-varying sigma depths), at each point and for each sigma vertical level, ROMS outputs are preliminarily interpolated onto the deepest sigma vertical level over the 2000–2008 period.

Once the solution of equation (2) is obtained, the alongshore current amplitudes (in a small wave number and low-frequency approximations) can be derived as follows:

$$v(x,y,z,t)=\sum_{n=1}^{\infty} G_n(x,z)\phi_n(y,t) \text{ with } G_n(x,z)=\frac{-1}{\rho_0 f}F_{nx}(x,z) \tag{4}$$

In order to compute the free CTW modal structures and CTW linear model parameters along the coasts of southwestern American and African continents, we applied a modified version of the Brink and Chapman (1987) Coastal-Trapped Wave programs which solve equation (2), using a technique based on resonance iteration approach (Brink, 1982; Wang & Mooers, 1976). For a given cross-shore section, providing the cross-shore topographic profile and the stratification vertical profile, they calculate the CTW mode structures ($F_n(x,z)$) as well as the associated phase speed (c_n). Calculus are performed at each cross-shore section along the coast of SEP and SEA, based on the model mean stratification and cross-shore bathymetric profiles of the twin ROMS configurations. We followed these steps:

1. Cross-shore topography: We first estimate the position of the coast in both ROMS domains using the model land mask. The alongshore direction is then computed based on a linear regression of the coastline over a 2° latitudinal window. At each latitude, the model topography is interpolated along each cross-shore section from the coast to a given maximum offshore distance (Xmax). According to Brink and Chapman (1987), Xmax is chosen such as it encompasses the continental shelf and slope. To satisfy this condition, the latter has been set to 200 km in the SEP and to 400 km in the SEA sector. Additional technical details are given in Figure 2.
2. At each latitude, ROMS mean potential temperature and salinity profiles over the 2000–2008 period are interpolated onto a regular 5 m vertical resolution grid over the whole water column. Then, offshore mean stratification vertical profiles ($N^2(x=X_{max},z)$) are computed from using the TEOS-10 formulation. Note that ROMS stratification remains fairly constant in the 400 km-width coastal band in both systems, supporting our choice of extracting the stratification at the offshore distance Xmax.
3. Pressure and alongshore current modal structures of the first four free CTW modes ($F_n, G_n, n=1\ldots4$) are derived at all cross-shore sections along southwestern American and African continents. For each coastal section, equation (2) is solved on a 100 terrain-following vertical levels, sampling the cross-shelf direction every 2 km.

4.2. Coastal-Trapped Wave Modal Decomposition

At a given latitude, knowing the vertical structure of the CTW modes and ROMS alongshore current and pressure along the associated cross-shore section, we aim at determining the amplitude of the gravest CTW modes ($\phi_n(y,t)$) which varies both along the coast and in time. At each location along the cross-shore section, the amplitude of the eigenfunctions should satisfy equations (1) and (4). In this section, we first recall the general principle and hypotheses of the technique introduced by Church et al. (1986a) to estimate CTW mode amplitudes from in situ observations. We then present our new methodology which allows inferring CTW amplitudes from model outputs.

4.2.1. Moore-Penrose Inversion Solution (ROMS^{INV})

The Moore-Penrose inversion approach is a semiempirical methodology developed by Church et al. (1986a) in order to infer CTW amplitude from sparse in situ observations. It is based on the inversion of a set of equation accounting for the fact that at each point (x,z) along a cross-shore section, the variability is reduced to the truncated sum of the gravest CTW modes. For instance, in Church et al. (1986a) or Yin et al. (2014), they estimated linear combinations of the first three CTW modes. Aside from CTW modes, Church et al. (1986a) also introduced a statistical offshore mode, in order to take into account the effect of the turbulent flow near the coast. This additional mode serves as a closure condition for resolving the sets of CTW mode equations, in absorbing energy associated with eddy activity. As opposed to CTW modes that have their maxima on the shelf and near the bottom, the offshore mode portrays a repartition of energy, with a maximum in the near-surface offshore region, which decays with depth and when approaching the shore. Church et al. (1986a) used exclusively in situ alongshore current measurements and one additional statistical offshore mode on which part of the energy can project onto. Yin et al. (2014) used SLA measurements concomitantly with alongshore current in situ data to estimate CTW mode amplitudes. They did not use any statistical offshore mode in their decomposition.

Here, we merge both approaches, using ROMS outputs as extended "virtual" measurements and allowing pressure and alongshore current fields to be used concomitantly. We use the four gravest CTW modes along with offshore statistical modes for pressure and alongshore currents. Further information about the implementation, along with equations, are provided in the Appendix A. In the following, this method will be referred to as the inversion methodology and labeled as **ROMS^{INV}**. This modal decomposition and its limitations will be discussed in section 6. However, the main objective of this paper is not to evaluate the skills of this methodology, but rather propose and validate our methodology adapted to CTW contribution from model output analysis. The latter is presented in the following section.

4.2.2. Projection Methodology (ROMS^{PROJ})

The projection methodology relies directly on the orthonormality condition of the pressure modal structures along the coast (at $x = 0$) and at the bottom ($z = 0$) (cf., equation (3)). Since, the pressure along a cross-shore section ($p(x,z)$) can be expanded as the infinite sum of orthogonal CTW modes (equation (1)), it follows that $p \otimes F_n = \left(\sum_m \phi_m F_m\right) \otimes F_n = \sum_m (\phi_m \delta_{mn}) = \phi_n$. Therefore, CTW mode amplitudes (ϕ_n) can be estimated such as:

$$\phi_n = \boldsymbol{p} \otimes F_n = f^{-1}\left(\int_{-h(0)}^{0} [\boldsymbol{p}\ F_n]_{x=0}\ dz + \int_{0}^{\infty} h_x [\boldsymbol{p}\ F_n]_{z=-h}\ dx\right) \tag{5}$$

Only the values of pressure and eigenfunction on the sloping shelf and at the coast are relevant for this calculus. They are available from model outputs, but rarely available in in situ data collected. Note however that the ROMS pressure values at the ρ-point closest to the coast (Figure 2) are assimilated to the coastal point (at $x = 0$).

This approach has the benefit of a simple formulation and implementation. In the following, it will be referred to as the projection methodology and labeled **ROMS^{PROJ}**.

4.3. Linear CTW Model

The above calculation provides information that will be used to tune a multimode linear CTW model. The latter is used for evaluating the skills of ROMS modal decomposition, as its solution will be compared to ROMS outputs. Following Clarke and Van Gorder (1986), CTW amplitudes should satisfy the solution of a simple Linear Coastal Model (LCM) of CTW propagations: each CTW mode n propagating poleward at the velocity c_n, forced by equatorial conditions ($\phi_n(y=0,t)$) and alongshore wind stress ($\tau^A(y,t)$). The effect of wind-stress

curl is assumed to be negligible, as the coastal boundary layer trapping scale is small relative to the alongshore length scales (Clarke & Brink, 1985; Clarke, 1977). The set of coupled first-order wave equations writes:

$$(\phi_n)_y - \frac{1}{c_n}(\phi_n)_t + a_{nn}\phi_n = b_n\tau^A - \sum_{\substack{m=1 \\ m\neq n}}^{+\infty} a_{mn}\phi_m \tag{6}$$

Without atmospheric excitation, CTW amplitude would decrease along their propagation due to bottom friction dissipation (a_{nn}). Modal scattering also occurs through a frictional coupling ($a_{\substack{mn \\ m\neq n}}$). The frictional decay and coupling coefficients are defined such as:

$$a_{nm} = rf^{-2}\left[\int_{-h(0)}^{0}\left[F_nF_{mx}h^{-1}\right]_{x=0}dz + \int_0^{\infty}F_n(x,-h)\frac{d}{dx}\left[rF_{mx}(x,-h)\right]dx\right] \tag{7}$$

with r the bottom friction coefficient (Clarke & Van Gorder, 1986).

The alongshore wind stress forcing is projected onto each CTW mode using the wind projection coefficient b_n, defined as:

$$b_n = \frac{1}{fh(0)}\int_{-h(0)}^{0}[F_n]_{x=0}dz \tag{8}$$

The model defined by equation (6) is integrated along the coast from its boundary conditions at the starting point (y = 0) and it is solved by the method of characteristics. In the algorithm developed by Clarke and Van Gorder (1986), CTW multimode linear model parameters (namely c_n, a_{mn}, and b_n) are a function of the latitude along the coast, accounting for the alongshore variations in bottom shelf topography and stratification.

We developed twin configurations of the LCM model along the SEP and SEA coasts. For the two systems, we use four CTW modes with their parameters (phase speeds, frictional coefficients, and wind projection coefficients) being estimated using the outputs of ROMS modal decomposition (cf., sections 4.1 and 5.1). CTW propagate poleward along the coastline (waveguide) defined from the twin ROMS configuration landmasks. According to the coastline curvature, LCM alongshore positions are estimated as the integrated distance (in km) from the equator along ROMS coastlines every 1/12°. The grid is then subsampled every 0.5° (labeled as model station positions), where coastal QuikSCAT alongshore wind-stress subseasonal anomalies and 0.5° latitudinal averages of CTW parameters are prescribed. To satisfy the LCM Courant-Friedrichs-Lewy stability condition (Clarke & Van Gorder (1986, equation (3.20)) with a 6 h time step, the model grid is divided into ∼5 km equidistant segments between two consecutive forcing stations. There, LCM linear interpolations of model parameters and wind-stress forcing are used. In the SEP (SEA), the model is integrated from the equator to 38.8°S (28.7°S), corresponding to 5,461 (3,819) km.

CTW modes are forced in the equatorial sector by the incoming long EKW (Clarke, 1983; Moore, 1968). At subseasonal frequencies, each EKW mode, forced in the western basin, reaches the eastern boundary at a different time and carries different time scales of variability. So, each EKW mode is considered as an independent forcing for coastal propagations. Here, we use the four gravest EKW modes contribution to SSLA estimated from SODA reanalysis (cf., section 2.3). In the Eastern Equatorial Pacific (Atlantic), EKW contributions are averaged within (105°W–95°W (5°W–5°E); 1°S–1°N), the most eastern location where the topography remains deep enough to accurately estimate the baroclinic modes. Time series are then shifted in time to account for the delay required by the wave to travel along the equator from this location to the eastern coast. In the Pacific (Atlantic) basin, accounting for the specific velocity of each EKW mode, we use a lag of 10, 22, 34, and 40 days (7, 12, 17, and 22 days) for EKW modes 1, 2, 3, and 4, respectively.

5. Results

In this section, we aim at disentangling the CTW contributions to the coastal variability from complex nonlinear dynamics simulated by high-resolution ocean models. Our final objective is to describe and explain the similarities and differences regarding the CTW dynamics and forcings of two systems that present different configurations, primarily in terms of the continental and shelf slopes (cf., companion paper, Illig et al.,

2018). In this context, we evaluate the skills of a new and relatively simple methodology that has never been tested out, the projection methodology (ROMS^{PROJ}, cf., section 4.2.1).

As a first step, we will use ROMS outputs (cross-shore topographic and stratification vertical profiles) to estimate the CTW modal structures along the southwestern American and African coasts from the Brink and Chapman (1987) formulation (cf., section 4.1 for the modal structure). Then CTW multimode linear model parameters (phase speed, frictional, and wind projection coefficients) will be derived and twin LCM configurations of the SEP and SEA (cf., section 4.3) will be developed. Next, CTW characteristics will be derived directly from ROMS outputs using the projection methodology detailed in section 4.2.2 (ROMS^{PROJ}). As the ROMS model includes nonlinear terms and diffusive processes, the comparison of ROMS CTW mode amplitudes with the solution of the simple LCM model will help evaluate if the modal decomposition of ROMS fields onto individual CTW modes behaves dynamically in a way similar to what is expected from linear theory (i.e., with CTW wave dynamics characterized by the phase speed, frictional, and wind projection coefficients estimated from ROMS outputs). This will provide a benchmark for evaluating the skills of ROMS^{PROJ} modal decomposition.

5.1. CTW Structures and Parameters

The first four free CTW modal structures have been estimated along each cross-shore section along the coast of SEP and SEA, every 1/12°, using a modified version of Brink and Chapman (1987) programs and based on ROMS mean stratification and cross-shore bathymetric profiles of the twin ROMS experiments (cf., section 4.1). Examples of CTW pressure (color shading) and alongshore-currents (contours) structures are shown in Figure 3 for cross-self sections along the Peruvian coast at 16°S and along the Namibian coast at 27°S. These latitudes were chosen because they are associated with contrasted CTW structures, nearly barotropic in the SEA and baroclinic in the SEP. According to the theory, the *n*th order CTW pressure mode at the coast and at the sloping shelf has *n* zero crossing(s). Note that numerical errors resulting in pockets of reversed sign in CTW pressure structures at the coast (Brink & Chapman, 1987) were avoided by using a quasi-flat topography between the coast and the closest ocean ρ-point in the ROMS grid (Figure 2). The baroclinicity of the CTW modal structures can be anticipated by calculating the Burger number $S=\alpha\bar{N}/f$ (Huthnance, 1978). It allows quantifying the relative importance of the latitude (through the Coriolis parameter *f*), the mean coastal vertical stratification ($\bar{N}$) and the cross-shore topography slope (α) on the nature of the CTW structures. Small *S* values correspond to fast CTW approaching barotropic continental shelf waves, while large *S* values are associated with slow-propagating baroclinic waves. The comparison between the two regions shows that the mean stratification (averaged over the first 3,000 m) remains almost constant along the coast and similar values are estimated in both systems (Figure 5 of the companion paper, Illig et al., 2018). As a consequence, in both regions, the shape of CTW modal structures is primarily controlled by the steepness of the continental slope divided by the Coriolis parameter *f* (see quantifications in the companion paper, Illig et al., 2018 in section 3.2 and Figure 5): Steep (gentle) topographic slopes are associated with baroclinic (barotropic) structures in the Humboldt (North Benguela) upwelling system, as illustrated on Figure 3.

Figure 4 presents the theoretical phase speeds (eigenvalues in equation (2)) at all cross-shore sections along southwestern American (plain lines) and African (dashed lines) continents for the first four CTW modes. Gravest CTW modes are faster than higher-order modes and CTW propagate faster in the SEA than in the SEP (Table 1), especially for latitudes higher than 20°S (Figure 4). In both systems and for each CTW mode, latitudinal variations of the wave velocity directly reflect the change in the nature of the CTW structures. In agreement with the Burger number formulation, the poleward increase in the Coriolis force is associated with more barotropic, faster CTW at high latitudes in both systems. This is reflected by the poleward gradual increase in CTW phase speed for all CTW modes and in both systems. The latitudinal changes in the wave velocity associated with changes in the coastal bathymetry and stratification are more noticeable for the first CTW mode (black lines in Figure 4). The higher the mode order, the smoother the latitudinal variation of the phase speed. For instance, the latitudinal variation in CTW mode 1 phase speed in the SEP clearly depicts the coastal wave acceleration associated with the broader (steeper) topographic shelf ($\alpha\sim20$ m.km^{-1}, $S^2\sim3.5$) in the northern Peru (~8°S) and their deceleration when encountering the abrupt bathymetry ($\alpha>50$ m.km^{-1}, $S^2>12$) off Pisco (at ~15°S). In the North Benguela upwelling system, the shallower and gentler bathymetry ($\alpha\sim5$ m.km^{-1}) yield a drastic increase in the CTW phase speed, associated with fast nearly barotropic CTW ($S<0.25$). Note that, the latitudinal variation of the CTW phase speed in the SEA hardly portrays the steepening of the bathymetry off the Angolan coast between 13 and 18°S. The

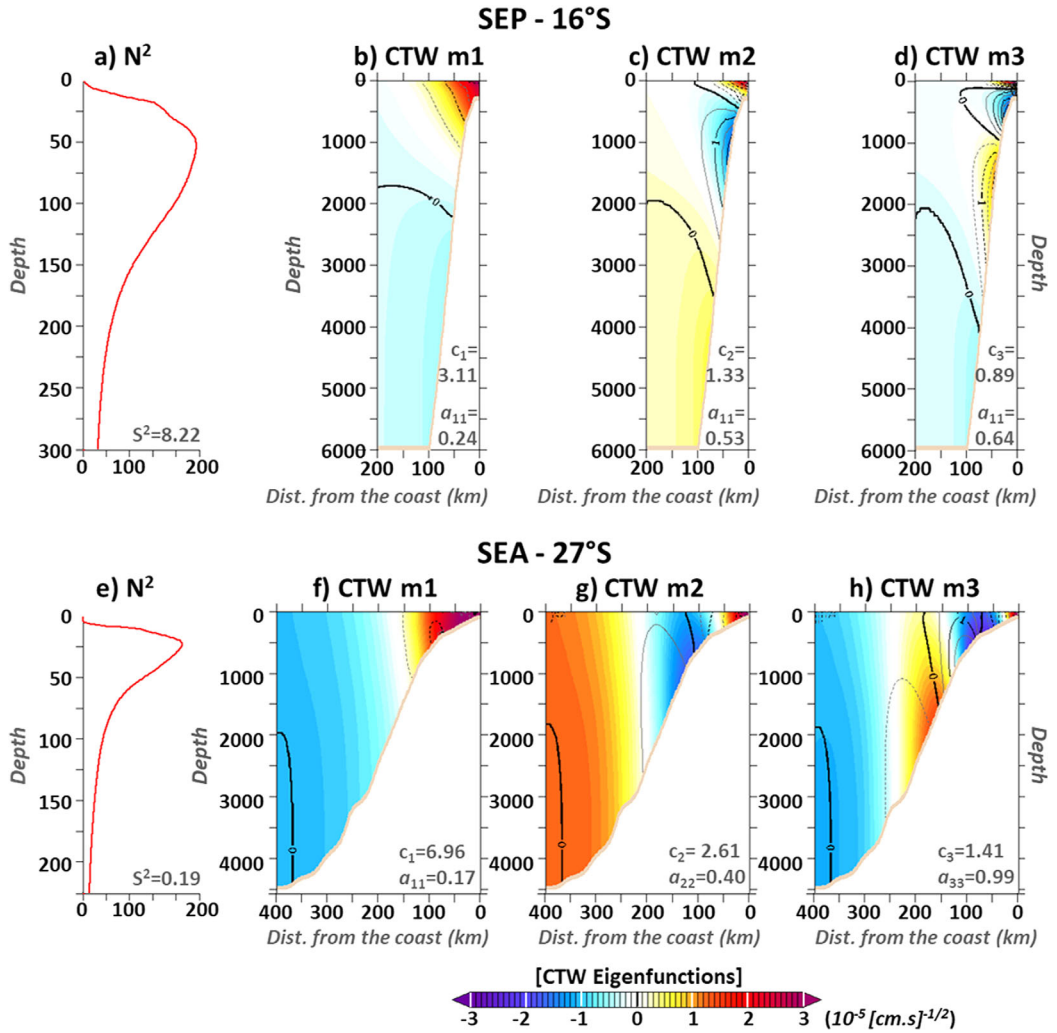

Figure 3. Stratification, eigenfunctions and eigenvalues along (top) the Peruvian coast at 16°S and along (bottom) the Namibian coast at 27°S. (left) The offshore Brunt-Väisälä frequency vertical profile ($N^2(x = x_{MAX})$ in 10^{-6} rad^2.s^{-2}), with stratification parameter (S^2) specified in the lower right corner. On the right are the first three theoretical CTW modal structures, with normalized pressure structures (F_n, in 10^{-5} (cm.s)$^{-1/2}$) in colors and associated alongshore velocity structures (v, $\times 100$) in contours. v structures are in arbitrary units which are consistent such as if p were in dyn/cm^2, v would be in cm.s^{-1}. The associated phase speed (c_n in m.s^{-1}) and dissipation coefficient (a_{nn} in 10^{-8} cm^{-1}) are listed in lower right corner of each subplots.

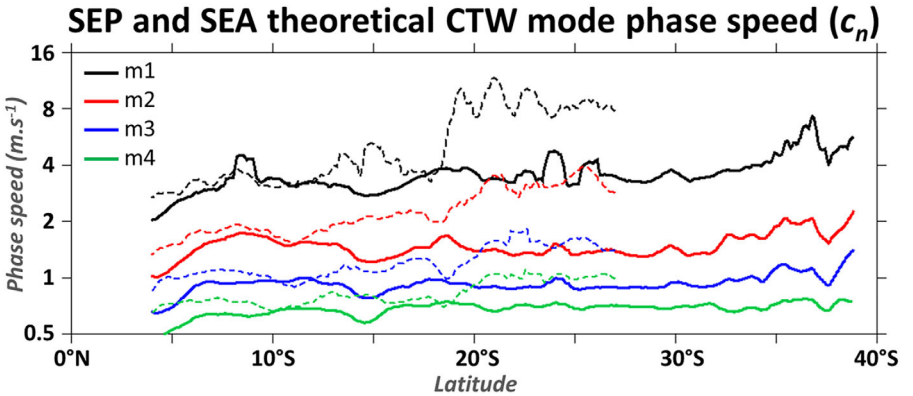

Figure 4. CTW theoretical phase speed (eigenvalues obtained from the CTW decomposition) in function of latitude along the coasts of the SEP (plain lines) and the SEA (dashed lines). CTW mode 1, 2, 3, and 4 are in black, red, blue, and green, respectively. Unit is m.s^{-1}. To better visualize fast and slower phase speed, we use a Log2 vertical scale.

Table 1
CTW Parameters Averaged Along the Coast

Sector	CTW parameters	CTW modes 1	2	3	4
SEP	c_n in (m.s^{-1})	3.62 $^{\pm 0.77}$	1.49 $^{\pm 0.19}$	0.93 $^{\pm 0.08}$	0.68 $^{\pm 0.04}$
(5°S–38°S)	a_{nn} in (10^{-8} cm^{-1})	0.32 $^{\pm 0.17}$	0.77 $^{\pm 0.29}$	1.19 $^{\pm 0.44}$	1.51 $^{\pm 0.51}$
	b_n in (10^{-2} (s.cm) $^{-1/2}$)	0.80 $^{\pm 0.38}$	0.63 $^{\pm 0.38}$	0.43 $^{\pm 0.32}$	0.21 $^{\pm 0.25}$
SEA	c_n in (m.s^{-1})	5.55 $^{\pm 2.60}$	2.34 $^{\pm 0.67}$	1.22 $^{\pm 0.24}$	0.83 $^{\pm 0.13}$
(5°S–27°S)	a_{nn} in (10^{-8} cm^{-1})	0.33 $^{\pm 0.12}$	0.78 $^{\pm 0.46}$	1.64 $^{\pm 0.66}$	2.00 $^{\pm 0.51}$
	b_n in (10^{-2} (s.cm) $^{-1/2}$)	0.88 $^{\pm 0.3}$	0.95 $^{\pm 0.49}$	0.80 $^{\pm 0.37}$	0.51 $^{\pm 0.25}$

Note. Sector and latitudinal average region, CTW parameters and their respective units, mean values for the four gravest CTW modes with latitudinal standard deviation indicated in superscript.

latter is actually compensated by the poleward decrease in vertical coastal stratification off Angola (Figure 5 of the companion paper, Illig et al., 2018).

From each CTW mode eigenfunction, frictional decay and coupling coefficients and wind projection coefficients are also estimated at each latitude following equations (7) and (8). Note that for simplicity and lack of information, the bottom friction coefficient remained constant with a value of 0.05 cm.s^{-1} (Brink & Chapman, 1987). The averaged values along the coast are listed in Table. 1. For each CTW mode, dissipation and modal scattering are more important in the SEA than in the SEP, along with the amplitude of the wind projection coefficients. Notably, south of 15°S and in both basins, local wind stress forcing will project preferentially onto the first CTW mode (*cf*. Figures 10c and 10d of the companion paper, Illig et al., 2018).

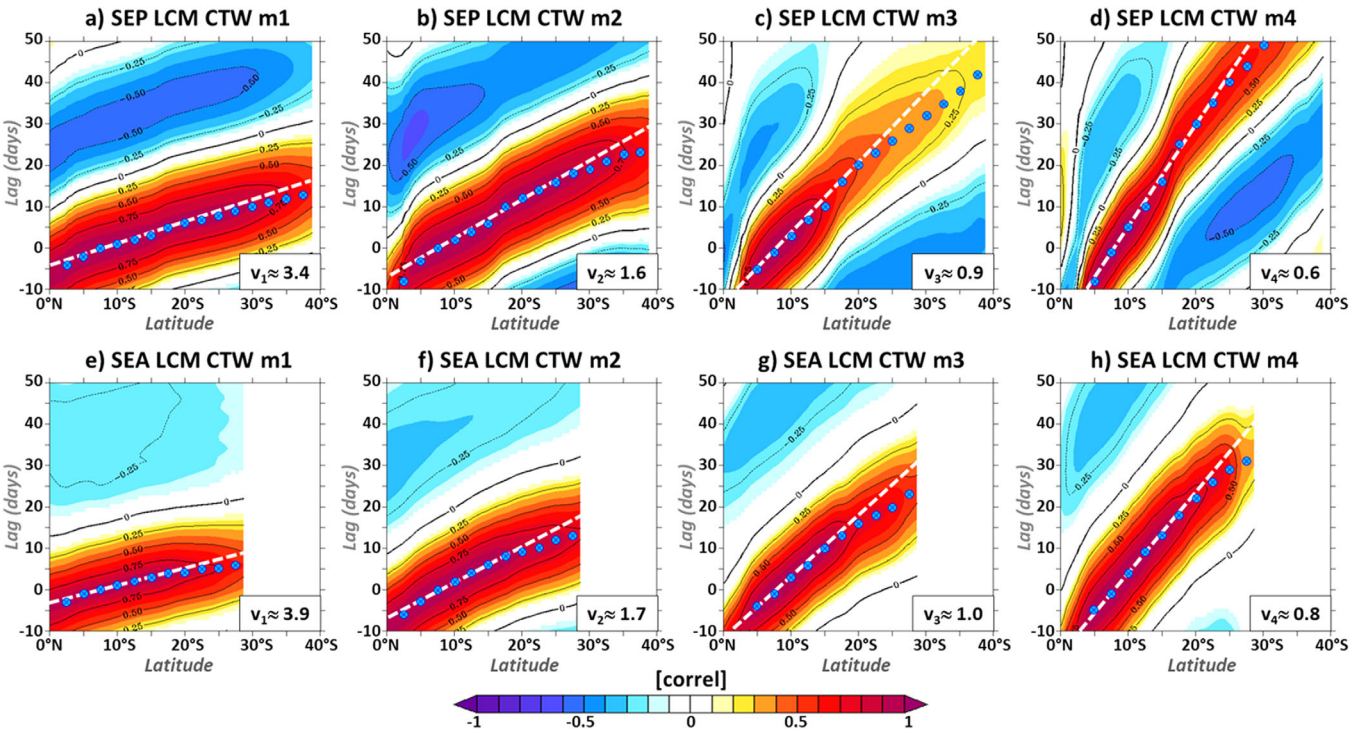

Figure 5. Lagged correlation between LCM CTW mode amplitude averaged between (7.5°S–8.5°S) time-series and LCM CTW mode amplitude at each latitude. Correlation coefficients are displayed as a function of the latitude along the coast and in function of the lag (in days), along the southwestern coasts of (top) South America and (bottom) Africa. Shading indicates correlation with a level of significance larger than 95% (Sciremammano, 1979). The analysis is performed for the four gravest CTW mode contributions (from left to right). Blue dots indicate the lag of maximum correlation in function of the latitude (every 2.5°). White dashed lines are the least-squares best-fit straight lines passing through the maximum correlation at each latitude. The associated slope or propagation velocity (in m.s^{-1}) is indicated in the lower right corner of each plot.

Hence, SEP and SEA coastal domains present distinct mean CTW vertical structures and parameters. They will thus provide different configuration setups to test the modal decomposition methodologies. In the following section, these theoretical CTW parameters will be used to parameterize CTW multimode linear model configurations along the coasts of SEP and SEA. The solutions will be used to provide a benchmark for the evaluation of the skills of ROMS output modal decomposition.

5.2. CTW Amplitudes From Multimode CTW Linear Model Simulations

We developed twin configurations of the LCM model as presented in section 4.3. The model is run over the 2000–2008 period and daily averages of CTW mode amplitude are saved at each model station.

We first performed a lag correlation analysis of the LCM CTW mode amplitude in order to infer the propagation velocity of each CTW mode in the SEP and SEA sectors (e.g., Figure 5 shows the results with a reference latitude at 8°S, similar to Figure 6 in Bachèlery et al., 2016a). In both systems, Figure 5 exhibits a clear low-frequency poleward propagating CTW wave signal, with relatively high correlation coefficients ($>$0.26) extending latitudinally over the whole basin. We quantified the propagating coherency by computing the maximum lagged covariance between the lagged-correlation values at 8°S and the one at all latitudes. Results are then normalized by the covariance estimated at 8°S. For both systems, propagating coherency values, averaged between 17°S and 27°S, are listed in Table 2. In agreement with the visual inspection of Figure 5, high coherence values ($>$0.8) are found for the fast CTW modes 1 and 2. CTW modes 3 and 4 are associated with lower coherence values ($<$0.6), which still remain high. The slope of the least squares best fit to the maximum correlation at each latitude (white dashed line in Figure 5) provides an estimation of the mean latitudinal speed of the CTW. The results obtained for each CTW mode (listed in the lower right corner of each subplot of Figure 5) remains in good agreement with the theoretical phase speed at ~8°S (Figure 4), with differences lower than 10%. Discrepancies are attributed to the fact that CTW are not free propagating waves: they are forced along their propagation by alongshore wind-stress and also because coupling between the different CTW modes occurs (equation (6)). We also observe a deflection of the high correlation patterns at high latitudes in the SEA (blue crosses in Figure 5), away from the linear slope of maximum correlations, and toward larger phase speed propagations. This is in agreement with the barotropic CTW properties of the Northern Benguela detailed previously (Figure 4).

LCM summed-up contribution of the four CTW modes to the subseasonal coastal variability is then compared to ROMS outputs. Figure 6 provides a Taylor diagram (Taylor, 2001), summarizing the agreement

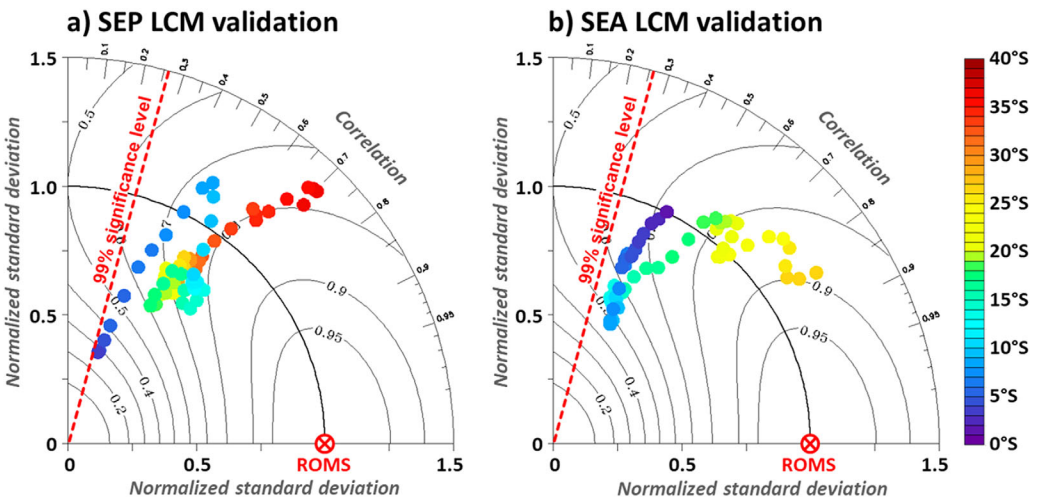

Figure 6. Taylor diagram illustrating the comparison between LCM and ROMS coastal (0.5° width band) SSLA over the 2000–2008 period at each latitude (specified by the color of the point) along the coasts of the (a) SEP and the (b) SEA. The radial coordinate gives the magnitude of total standard deviation, normalized by the one of ROMS value, and the angular coordinate gives the correlation. It follows that the distance between the reference point (ROMS, red strikethrough circle) and any LCM point is proportional to the RMS difference between ROMS and LCM coastal SSLA. Isolines provide a measure of the skill as defined by equation (4) from Taylor (2001). Dashed radius line denotes the limit of the 99% significance level for the correlation (Sciremammano, 1979).

Table 2
Propagating Coherence Estimated From CTW Amplitude Lagged-Correlation Analysis With LCM (Figure 5), ROMS^{PROJ} (Figure 8), and ROMS^{INV} Outputs, for the Southeastern Pacific (Atlantic) Sector, Averaged Between 17°S and 27°S (in brackets)

	CTW modes			
	1	2	3	4
LCM	**0.94** (**0.83**)	**0.92** (**0.85**)	**0.51** (**0.59**)	**0.59** (**0.55**)
ROMS^{PROJ}	**0.89** (**0.71**)	**0.64** (**0.52**)	0.39 (0.43)	0.12 (0.22)
ROMS^{INV}	**0.65** (**0.58**)	0.34 (**0.50**)	0.14 (0.03)	0.09 (0.11)

Note. Coherence values larger than 0.5 are in bold. See sections 5.2 and 5.3 for further details on the calculation of the coherence.

between LCM and ROMS coastal (0.5° width band) SSLA time series at each latitude along the coast every 0.5° (color of the points). In this polar plot, the azimuthal angle provides a measure of the correlation (R) between LCM and ROMS SSLA time series. The radial distance from the origin (r) to any point is the ratio of LCM Root Mean Square (RMS) to that of ROMS. ROMS point, marked with a red strikethrough circle, is located at (R = 1; r = 1). The distance from any point to ROMS point is equal to the normalized error (ratio of the RMS difference between LCM and ROMS coastal SSLA to the RMS of ROMS time series). Given the time scales of ROMS and LCM coastal subseasonal SLA, we estimated that the 2000–2008 daily time series have a minimum of 150 degrees of freedom (following Sciremammano, 1979). As a result, the threshold of the 99% significance correlation is 0.26. It is represented by the red dashed radius line in the diagrams. The comparison between LCM and ROMS indicates that LCM solutions agree well with ROMS coastal SSLA in both systems, with adequate levels of energy and correlation coefficients significant at a 99% level for each latitude. This highlights the importance of the CTW dynamics on the observed SSLA variability in the SEP and the SEA sectors, associated with the subseasonal equatorial forcing and with the local wind-stress fluctuations. Notably, LCM is more skilful at higher latitudes, in particular in the North Benguela upwelling system (Figure 6b), where the coastal dynamics responds to the local wind forcing (Goubanova et al., 2013; Hormazabal et al., 2001; companion paper, Illig et al., 2018). The marginally lower agreement in the equatorial band is most likely due to the simplified formalism of the LCM that is not able to reproduce the complex processes associated with the coastal dynamics simulated by ROMS. In particular, the reflection of the EKW into equatorial Rossby waves and the radiation of extra-equatorial Rossby waves, along with the nonlinear dynamics associated with the subseasonal mesoscale activity, is not represented in the LCM. Note that the LCM skills could be improved by tuning the bottom friction coefficient *r* which controls the amplitude of the model frictional coefficient (equation (7)). It is reminded that in our twin configuration of the LCM, *r* is kept constant and equal to 0.05 cm.s^{-1} in both systems and at all latitudes (cf., section 5.1).

The overall good agreement between ROMS and LCM coastal SSLA in both systems also gives confidence in the LCM solutions to provide a guideline for the assessment of CTW mode amplitude estimated from ROMS modal decompositions. In this context, top plots of Figure 7 present the amplitude of each LCM CTW mode along the coast of southwestern American and African continents, in terms of coastal SSLA RMS. Results show that the SEP and SEA systems exhibit different relative contributions of each CTW modes at subseasonal timescales. In the SEP, the first CTW mode is the most energetic all along the coasts of Peru and Chile (in agreement with the hypothesis of Brink, 1982), while CTW mode 2 carries ∼50% less energy than CTW mode 1 (Figure 7a). CTW modes 3 and 4 have minor contributions. Conversely, in the SEA, the dynamics appears to be more complex, with a predominance of the second CTW mode from the equator to 13°S, while further poleward the first CTW mode is the most energetic (Figure 7b). This is in agreement with the coastal propagation velocities estimated by Polo et al., (2008). North of 20°S, higher-order CTW modes (mode 3 and 4) have a substantially larger contribution to the coastal variability than that in the SEP. The differences between the two systems in terms of dynamics and forcings are further discussed in the companion paper (Illig et al., 2018). For this study, Figures 7a and 7b provide a useful guideline for the amplitude of each CTW mode contribution in the two systems showing relatively different CTW dynamics. It should be kept in mind that LCM has a simplified formulation which can account for some divergence between LCM and ROMS or between LCM and observations. Also, differences between the two systems will provide a sensitivity test for the evaluation of the modal decomposition methodologies.

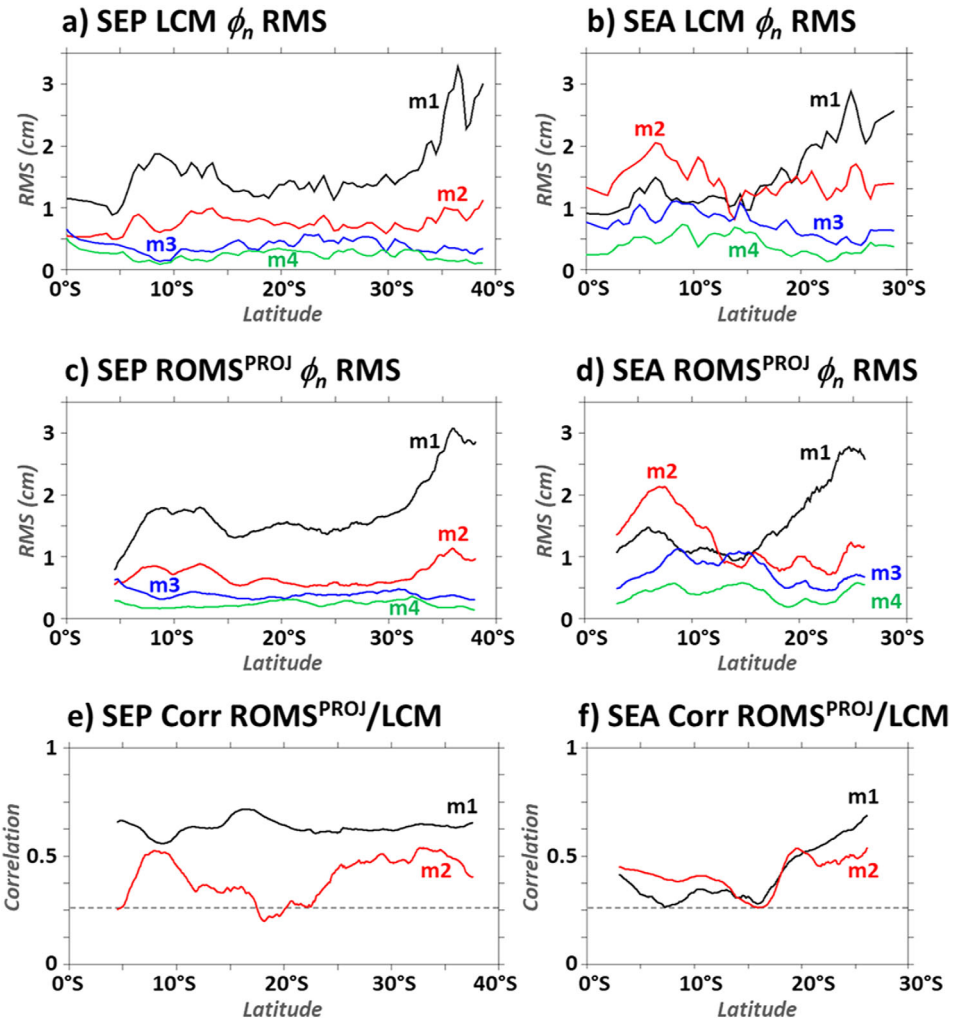

Figure 7. RMS of CTW mode contribution to coastal (0.5° width band) SSLA for (top) LCM and (middle) ROMS^{PROJ} solutions, in function of the latitude along the coast. Unit is cm. Correlation coefficients between SSLA from ROMS^{PROJ} and LCM for the two gravest CTW modes are displayed on the bottom plots. Dashed horizontal lines denote the limit of the 99% significance level for the correlation (Sciremammano, 1979). CTW mode 1, 2, 3, and 4 are in black, red, blue and green, respectively, and analyses along the southwestern coast of South America (Africa) are displayed in the left (right) plots.

5.3. Subseasonal CTW Mode Contribution to Model Coastal Variability

In this section, the skills of our new modal decomposition technique (presented in section 4.2.2) are evaluated in the light of the results obtained with the linear CTW model solutions and against expected theoretical CTW characteristics. The amplitude of the first four CTW modes is thus estimated using ROMS model pressure field along each cross-shore section in both systems based on the projection onto the CTW eigenfunctions (equation (5)). Time series are then filtered in order to retain only the subseasonal frequencies.

We first compare the amplitudes of each ROMS^{PROJ} subseasonal CTW mode to the solutions of LCM simulations. The middle plots of Figure 7 present the magnitudes of the four gravest CTW mode contributions to coastal SSLA that are estimated using the projection methodology for the SEP (left plots) and the SEA (right plots) coastal fringes. Results show that in both basins the amplitude of CTW modes derived from ROMS outputs using ROMS^{PROJ} methodology (Figures7c and 7d) and the LCM outputs (Figures 7a and 7b) are in very good agreement. ROMS^{PROJ} outputs indeed capture the level of energy of each CTW mode and the main characteristics of each system as simulated by the LCM. In the SEP, CTW mode 1 is the most energetic with a poleward increase in amplitude (coastal SSLA RMS) from ∼1.75 cm at ∼10°S to larger than 2.5 cm

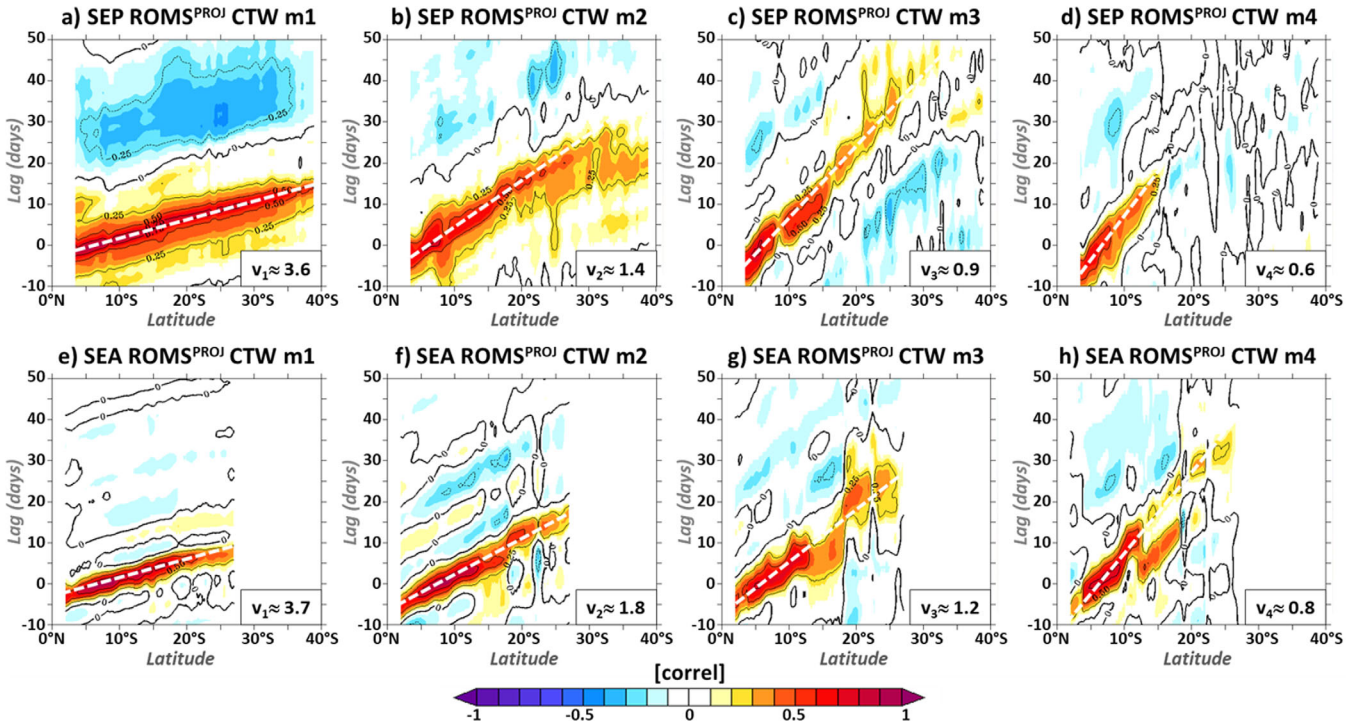

Figure 8. Same as **Figure 5** but for ROMS^{PROJ} CTW mode amplitude.

south of 34°S (Figures 7a and 7c). In the SEA, our new methodology depicts the transition between the dominance of the second CTW mode north of 13°S (CTW mode 2 coastal SSLA RMS >2cm at ∼7°S) and the control of the variability by the first CTW mode further poleward (CTW mode 1 coastal SSLA RMS >2.5 cm at ∼24°S) (Figures 7b and 7d). The amplitudes of the higher-order CTW mode are also in good agreement between the two estimations. The comparison between ROMS^{PROJ} modal decomposition and LCM outputs is further examined by computing the correlation between ROMS^{PROJ} and LCM coastal SSLA. Results are displayed in Figure 7e for SEP and Figure 7f for SEA. For the two gravest subseasonal CTW modes, there is a good agreement between ROMS^{PROJ} and LCM outputs, with significant correlation coefficients (>0.26) all along the coast in both systems. However, the correlation coefficients between ROMS^{PROJ} and LCM outputs are not significant for modes 3 and 4 (not shown). The discrepancies between ROMS^{PROJ} and LCM will be discussed in the following section.

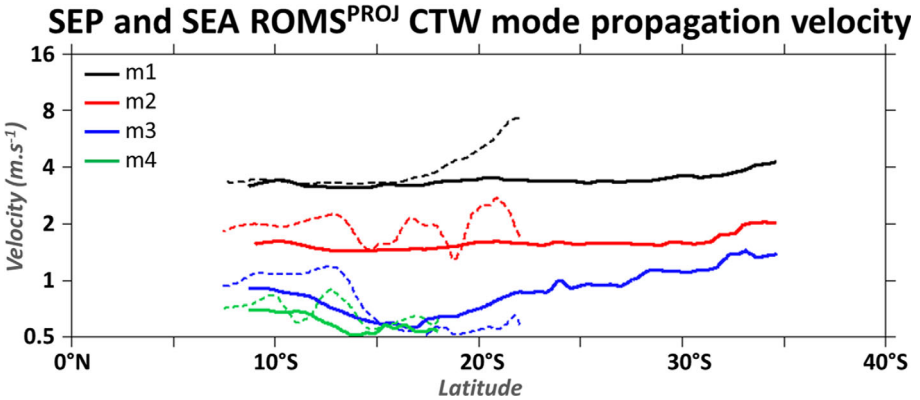

Figure 9. Similar to **Figure 4**, but CTW mode propagation velocity (m.s^{-1}) are estimated from ROMS^{PROJ} CTW modes amplitude. For each CTW mode and each latitude, propagation velocity is estimated by linear regression that best fits the maximum lagged correlation analysis within a 5° latitudinal window (similar to **Figure 8**).

To further evaluate the skills of our projection methodology, we estimated the propagating characteristics of ROMS inferred CTW mode contributions. In order to estimate the propagation velocity of each CTW modes in SEP and SEA sectors, we performed the same lag correlation analysis as the one estimated with LCM outputs (Figure 5) but, instead using ROMS^{PROJ} CTW mode contributions to coastal SSLA. Results, displayed in Figure 8, exhibit a clear signature of CTW propagation along the coast of SEP and SEA, with high coherency (correlation $>$ 0.26) extending latitudinally quite far south. In particular, the two gravest CTW modes exhibit a significant correlation which extends to the southern boundary of our domain. Correlation patterns are in fair agreement with the results obtained with LCM outputs (Figure 5), however narrower bands of significant and positive correlations are evident and most likely associated with ROMS nonlinear coastal mesoscale dynamics. Propagating coherencies have been quantified using a covariance analysis along the line that best fits the maximum correlation (dashed lines in Figure 8). Coherency estimations averaged between 17°S and 27°S are listed in Table 2 for each CTW mode and for the two systems. Values are considerably lower than the ones obtained with LCM outputs but remain high for CTW modes 1 and 2. CTW modes 3 and 4 are significantly less coherent, which differs from LCM outputs. As mentioned before, discrepancies associated with high order CTW modes may be due to the simplified LCM dynamics. CTW propagating velocities are then estimated based on the slope of the least squares best fit to the maximum

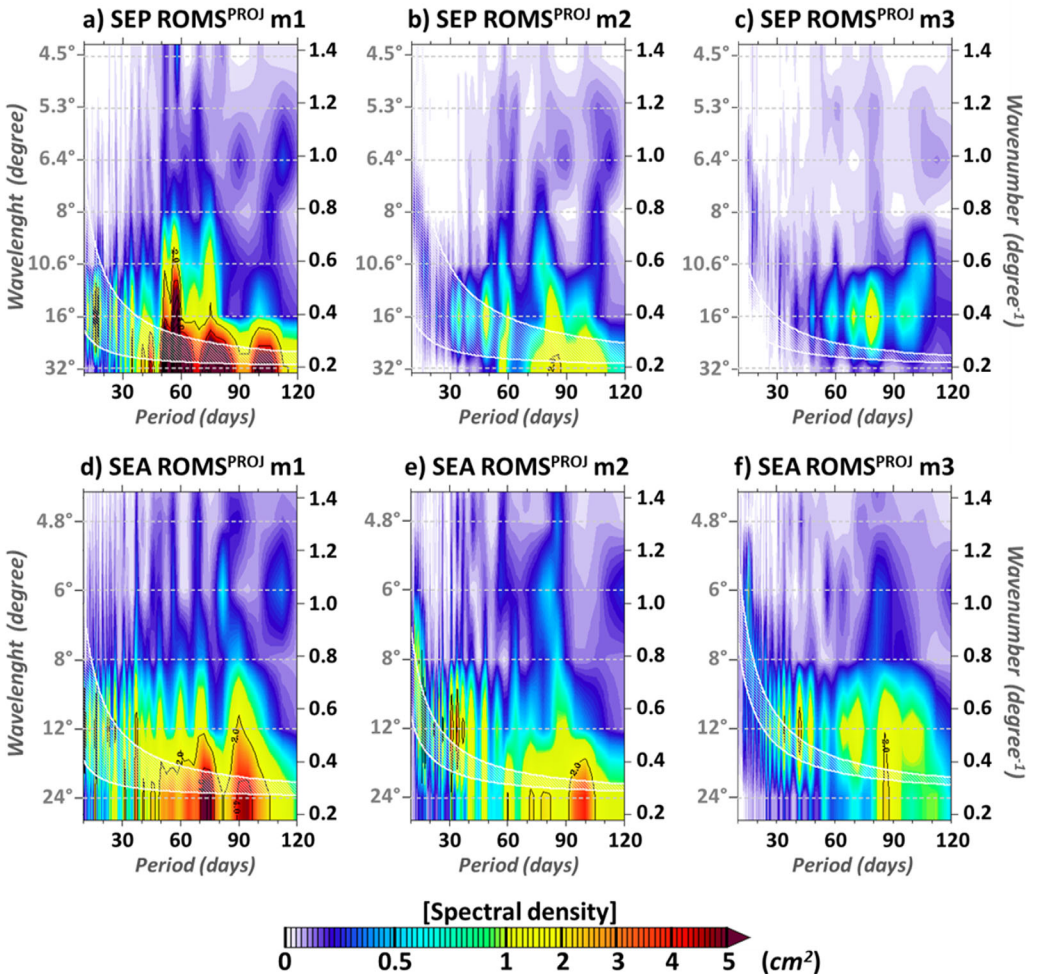

Figure 10. Space-time power spectral density (Hayashi, 1982) of ROMS^{PROJ} CTW modes contribution to coastal SSLA, in (top) the SEP and (bottom) the SEA for the (left) first, (middle) second, and (right) third CTW mode as function of wavelength (degree, left scale) or wavenumber (degree^{-1}, right scale) and period in days (bottom scale). In the SEP (SEA), the analysis is performed within a 32° length (24° length) coastal band extending from 3°S to 35°S (3°S–27°S) and spectra are calculated for the wavelength/wavenumber indicated with horizontal dashed lines. Units are cm^2. Hatched area indicates a range of theoretical dispersion curves estimated using the latitudinally averaged phase speed ± 1 standard deviation listed in Table 1.

correlation and are listed in lower right corner of each plot in Figure 8. Results indicate that the projection methodology successfully extracts poleward propagating CTW modes with phase speeds close to the theoretical ones for the four gravest CTW modes and in the two basins. Indeed, discrepancies between ROMS^{PROJ} CTW mode velocity and the one estimated with LCM outputs using the same methodology (Figure 5) are lower than 20%. Finally, phase speeds are estimated at all latitudes along the coast, fitting the best line through the scattered plot of the lag that maximizes the correlation between the CTW mode amplitude at a given latitude and the ones within a 5° centered latitudinal window versus the distance from the central point. Results are displayed in Figure 9 for the four gravest CTW modes and for the SEP (plain lines) and SEA (dashed lines) sectors. The obtained values are in very good agreement with the theoretical ones (Figure 4). Indeed, they exhibit the larger phase speeds of the SEA compared to SEP and they also nicely capture the acceleration of the wave with the latitude that is associated with the increased Coriolis force in both systems and with the barotropic CTW associated with the gentle bathymetry in the North Benguela upwelling system.

Finally, the frequency characteristics of ROMS^{PROJ} CTW in the SEP and SEA are further investigated from a space-time spectral analysis (Hayashi, 1982) applied to the contributions of the three gravest CTW modes to SSLA. The resulting wavelength-frequency diagrams (Figure 10) show the rich spectrum of energy of long-wavelength (>8° of latitude) at subseasonal timescales. It also highlights the signature of CTW propagations since the dominant density peaks fit the theoretical dispersion curves (hatched area). The latter are derived from the CTW mode decomposition based on the latitudinally averaged phase velocity listed in Table 1. The results presented in Figures 8–10 give confidence in the ability of the projection methodology to disentangle CTW mode contributions from complex nonlinear coastal processes that control the coastal subseasonal variability.

6. Discussion and Conclusions

In this paper, we introduce a new CTW modal decomposition technique based on a simple projection of coastal and along-shelf bottom pressure onto CTW vertical structures. This method benefits from a relatively simple implementation and is adapted to ocean model outputs. To derive CTW characteristics along the southwestern coast of the South American and African continents, we developed twin configurations of the ROMS model that reproduces the variability fairly well. Model outputs allowed testing this methodology in two coastal environments that present distinct characteristics in terms of types of CTW structures ranging from baroclinic waves confined along the steep topographic slopes of the Humboldt system to nearly barotropic waves in the North Benguela upwelling system. Focusing on subseasonal timescales, we were able to extract the gravest CTW wave mode contributions with propagating characteristics that are remarkably consistent with theoretical values. In the SEP, the estimated CTW parameters are in agreement with the study of Brink (1982). To our knowledge, this is the first time that CTW contributions to the coastal subseasonal variability have been derived and described in the SEA. As no estimation exists over the 2000–2008 period, we relied on the solutions of a simple multimode linear CTW model tuned with CTW characteristics inferred from ROMS CTW modal decomposition to further validate the derived CTW amplitudes in both regions. We found a relatively good agreement between ROMS modal decomposition and the LCM outputs. Notably, some discrepancies were reported, especially for the nondominant high-order modes. On the one hand, they may be attributed to the physics of the LCM that can somehow be too simplified to realistically simulate the dynamics of high order CTW modes. For instance, we did not take into account the interactions between CTW and the mean alongshore flow or seasonal to interannual variations of the ocean stratification in the LCM implementation, which can impact the phase speed of the CTW, changing the timing of the coastal waves and thus decreasing the correlation between ROMS and LCM. Likewise, for simplicity purposes, we chose to not include in the LCM formulation the CTW modal scattering due to the change in the shape of CTW wave structures from one latitude to another, as introduced by Johnson (1991) and implemented by Jordi et al. (2005). Also, ROMS nonlinear coastal mesoscale features can also erroneously project some energy onto the CTW structures, which will limit the agreement with the linear model. This could be tested by running noneddy-resolving ROMS simulations (by linearization of the momentum equation) as conducted in Gruber et al. (2011). However, this is not within the scope of the present study. In conclusion, in light of our validation exercise, we are confident that the proposed modal decomposition allows for disentangling CTW contribution from the complex coastal processes that control the coastal variability.

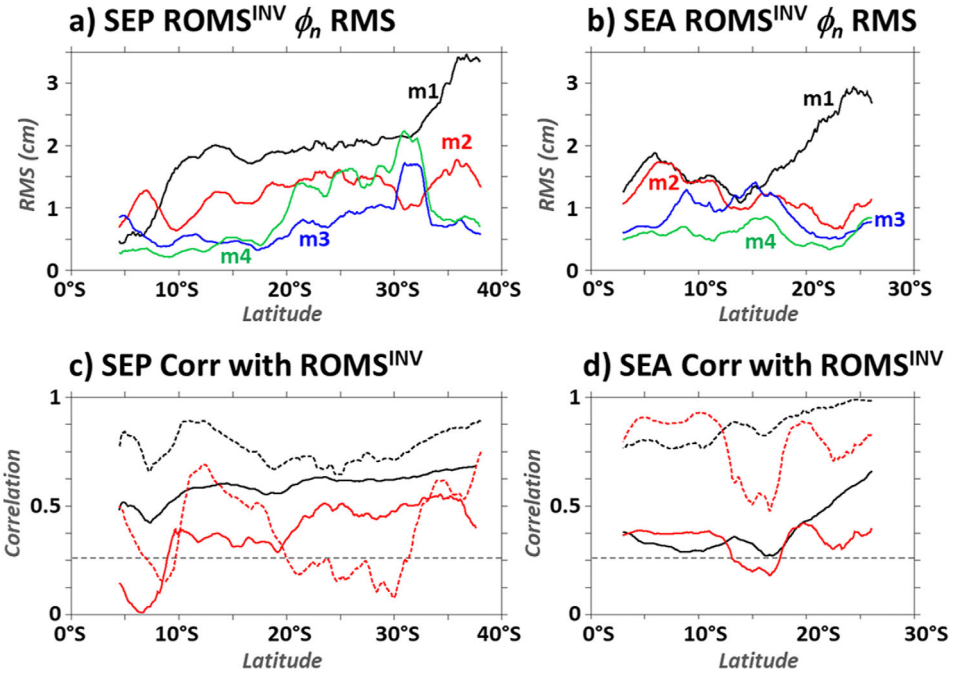

Figure 11. (top) RMS of CTW mode contributions to coastal (0.5° width band) SSLA for ROMS^{INV} solutions, in function of the latitude along the coast. Unit is cm. (bottom) Correlation coefficients between CTW mode amplitudes from ROMS^{INV} and LCM (ROMS^{PROJ}) in plain (dotted) lines for the two gravest CTW modes in function of the latitude along the coast. Dashed horizontal lines denote the limit of the 99% significance level for the correlation (Sciremammano, 1979). CTW mode 1, 2, 3, and 4 are in black, red, blue and green, respectively, and analyses along the southwestern coast of South America (Africa) are displayed in the left (right) plots.

Our methodology is best suited for the modal decomposition of high-resolution ocean model outputs that provide pressure information where CTW vertical structures are orthonormal (i.e., at the coast and on the sloping shelf, see equation (3)). Using in situ observations, Church et al. (1986a) developed a semiempirical methodology in order to infer CTW amplitude from fixed mooring data array, in which the variability observed within the coastal fringe is explained by the gravest CTW modes and one statistical offshore mode. This methodology (ROMS^{INV}) is presented in section 4.2a and our implementation is detailed in the Appendix A. To our knowledge, this technique is the only methodology that allows deriving CTW amplitude from in situ observations. However, the main drawback of this methodology lies on the fact that the coastal variability has to be reduced to the sum of the gravest CTW modes. This can result in an incorrect linear combination of CTW modes, because all that is taken into account is that their summed-up contribution best fits the coastal variability. This is all the more true in regions where the coastal dynamics is not governed to a large extent by CTW propagations, even if projecting part of the energy onto additional statistical offshore modes can reduce this problem. However, this methodology was originally developed in order to estimate CTW amplitude using a finite array of data from fixed mooring lines, whose observation points were located where CTW modes are not orthogonal (Church et al., 1986a; Yin et al., 2014). It showed some skill for the interpretation of the coastal variability in terms of CTW propagations in the Australian Coastal experiment (Church et al., 1986a, 1986b), in the East China Sea (Yin et al., 2014) and in the Bay of Biscay (M. Kersalé, personal communication, 2017). For completeness, it is interesting to succinctly evaluate here the extent to which the ROMS^{INV} technique yields consistent results with our projection methodology and with the solutions of the LCM. Therefore, considering ROMS model outputs as an extensive set of measurement points, the skill of ROMS^{INV} modal decomposition can be evaluated in various configurations (bathymetry profile, stratification, CTW mode contributions).

We first estimated CTW contributions using the maximum available model pressure and alongshore current subseasonal anomalies along each cross-shore section by arithmetically inversing the Moore-Penrose set of equations (Appendix A, equation (A1)). Derived CTW subseasonal amplitudes are compared to LCM and

Table 3
CTW Mode Amplitude From LCM, ROMS^{PROJ} and ROMS^{INV} Sensitivity Experiments to the Type of Input Data Considered (pressure p and/or alongshore current v), Their Location Within Cross-Shore Sections Along the Coasts, and the Eventual Use of Offshore Statistical Modes

Modal decomposition technique				SEP around 25°S (off Chili)						SEA around 11°S (off Angola)					
				% Exp. Var.			Taylor Score			% Exp. Var.			Taylor Score		
				m1	m2	m1-4	m1	m2	m1-4	m1	m2	m1-4	m1	m2	m1-4
LCM				73	31	100	100	100	100	10	38	100	100	100	100
ROMS^{PROJ}				59	22	78	80	43	80	17	54	87	62	50	55
ROMS^{INV} sensitivity tests															
Use of *p*	Use of *v*	Use of Stat. modes	Cross-shore input data location												
✓	✓	✓	All available	56	-87	83	70	40	51	44	61	93	64	49	49
✓	✓		All available	66	-57	39	78	35	41	39	63	97	66	60	43
✓		✓	All available	53	-79	74	70	65	48	37	51	94	61	55	47
✓			All available	59	-85	18	76	33	36	33	43	94	66	56	47
	✓	✓	All available	52	23	54	74	52	62	31	49	63	57	41	38
	✓		All available	48	16	54	76	53	62	30	49	63	57	41	37
✓	✓		Coast + Bottom	78	32	95	79	20	68	30	58	98	33	46	47
✓			Coast + Bottom	71	-2	94	83	46	71	27	52	98	46	46	47
	✓		Coast + Bottom	18	-26	-39	27	32	22	0	4	5	0	18	27

Note. Results were averaged within (24°S–26°S) off the Chilean coast and within (12°S–10°S) along the Angolan coast. Results include the explained variance of CTW mode 1, mode 2, and the explained variance of the summed-up contribution of the first four CTW modes. CTW mode 1, mode 2, and the summed-up contribution of the first four CTW modes are compared to LCM solutions using Taylor score as defined by 100 × equation (4) from Taylor (2001). Green (orange) cell shading highlights modal decomposition results for which the explained variance of the summed-up contribution first four CTW modes is larger (lower) than 70% (40%) or a Taylor score between LCM and ROMS modal decomposition larger (lower) than 70 (60) for the summed-up contribution of the first four CTW modes.

ROMS^{PROJ} solutions in Figure 11. Results show that in both basins the amplitude of CTW mode 1 from ROMS^{INV} (Figures 11a and 11b) is in good agreement with the amplitude of LCM (Figures 7a and 7b) and ROMS^{PROJ} (Figures 7c and 7d) CTW mode 1. ROMS^{INV} CTW mode 1 solution slightly differs from LCM outputs at lower latitudes, exhibiting less (more) variability in the SEP (SEA). In the SEA, the two methodologies provide a similar level of energy for each CTW mode. North of 10°S, the amplitude of CTW mode 2 is however slightly underestimated in ROMS^{INV} compared to the LCM reference. In the SEP, the amplitudes of CTW modes 2 to 4 are substantially larger in ROMS^{INV} solution than in ROMS^{PROJ} and LCM solutions. The correlation coefficients between ROMS^{INV} and LCM and between ROMS^{INV} and ROMS^{PROJ} subseasonal CTW amplitudes (Figures 11c and 11d) further confirms that both methodologies provide similar results, in agreement with the LCM outputs, for the dominant CTW modes: CTW mode 1 in the SEP and CTW modes 1 and 2 (north of 13°S) in the SEA. We note however that ROMS^{PROJ} CTW SSLA are in better agreement with LCM outputs than the one of ROMS^{INV}. Finally, the analysis of the propagating characteristics of ROMS^{INV} CTW modes reveals significantly less coherent signals along the coast than for LCM and ROMS^{PROJ} solutions (Table 2). The estimated propagating velocities (not shown) are in good agreement with the theoretical CTW phase speeds of the dominant CTW modes, but unlike ROMS^{PROJ} analysis, incoherent values are estimated for modes 3 and 4 in both systems and for mode 2 south of 18°S in the SEP. This can be attributed to the limitations of ROMS^{INV} methodology discussed above, i.e., erroneous high-order CTW mode amplitudes associated with the arithmetic inversion of an overdetermined set of equations. Also, it is important to point out that ROMS^{INV} modal decomposition is performed using model inputs and eigenfunction values interpolated on ROMS grid (1/12°–37 vertical levels). This grid is coarser than the resolution at which CTW spatial structures are computed (2 km; 100 vertical levels), and the CTW structures do not fully satisfy the eigenfunction orthonormality condition (equation (3),

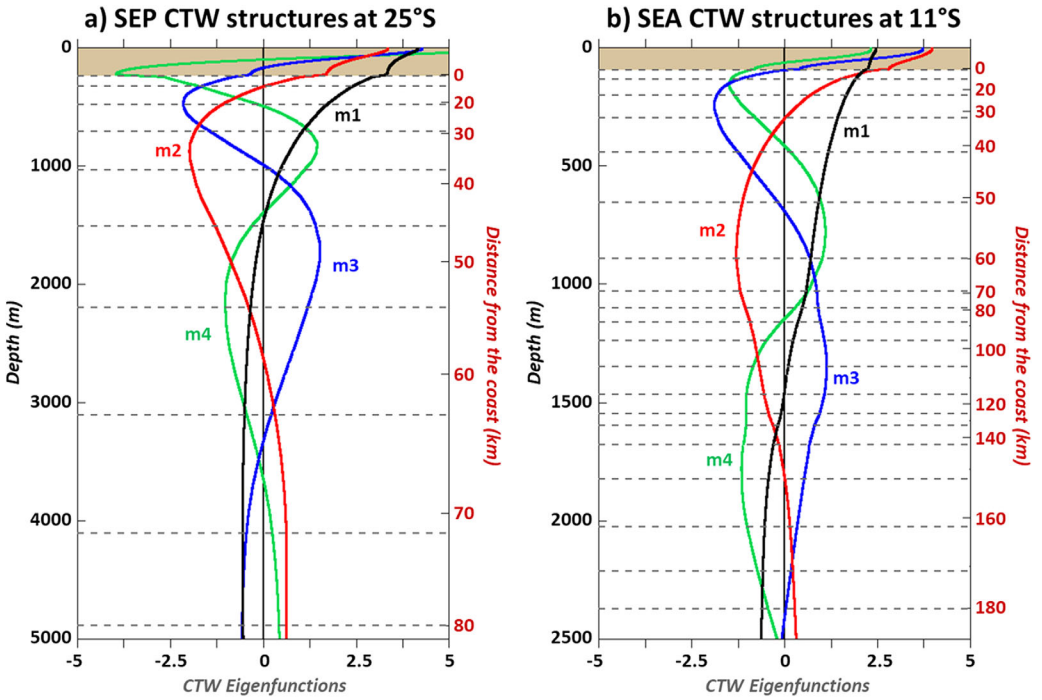

Figure 12. CTW eigenfunctions (F_n in 10^{-5} $(cm.s)^{-1/2}$) at the coast (brown shading) and along the bathymetry, as a function of depth (left scale) and cross-shore distance (right scale). Left (right) plot shows F_n values off the Chilean coast at 25°S (Angolan coast at 11°S). CTW mode 1, 2, 3, and 4 are in black, red, blue and green, respectively. Horizontal dashed grey lines indicate the location of the center of ROMS w-grid cells along the bathymetry. For readability, the 38 ROMS points sampling the water column at the coast are not shown.

Brink, 1989). For a given cross-shore section, the product between CTW eigenvectors should remain close to zero for $m \neq n$ and close to one for $m=n$. Maximum differences (∼30%) were indeed obtained along the steep continental slope along the coast of Northern Chile. Notably, differences lower than 5% are estimated in the Benguela upwelling system, where a gentler bathymetry is encountered.

We also briefly carried out sensitivity experiments to the type of input data considered in ROMS^{INV} modal decomposition (pressure and/or alongshore current), their location within cross-shore sections along the coasts of SEP and SEA, and the use of off-shore statistical modes. As an example, we present some results conducted using ROMS outputs at ∼25°S off Chile and along the coast of Angola at ∼11°S. These locations were chosen because they correspond to the latitude at which the remote equatorial forcing fades out in the analysis of subseasonal coastal SLA (cf., companion paper, Illig et al., 2018) and also because two moorings have been deployed at ∼11°S in the SEA (Kopte et al., 2017). Note also that we implemented the inversion technique with four CTW modes (cf., Appendix A). It is most likely that including more CTW modes in the Moore-Penrose system would impact the obtained solutions. However, this is beyond the scope of our objectives to test all the possible scenarios. Results are summarized in Table 3, in which LCM solutions are regarded as the reference. Table 3 reveals that using the maximum available pressure data concomitantly with alongshore current data results in CTW amplitudes in better agreement with LCM and ROMS^{PROJ} outputs. In both systems, pressure data appear to be more valuable than alongshore current data to infer realistic gravest CTW modal amplitudes. In the SEP, the inclusion of offshore modes in the Moore-Penrose system appears to be instrumental to infer a suitable solution. In the SEA, our statistical mode might be slightly too offshore to absorb a significant amount of energy. As expected from the orthonormality properties of the CTW eigenfunctions (cf., section 4.1 and equation (3)), pressure data along the bathymetry and at the coast are sufficient to capture the gravest CTW mode signature. The number of data could even be decreased by selecting particular locations to build a well determined system of equations. It would require inspecting the values of the pressure structures of the gravest CTW modes, where they form a complete set, i.e., at the coast and along the bathymetry. Positions where particular CTW eigenfunctions encounter

maximum amplitudes and where others pass through nodes should be depicted. An example is given in Figure 12 which overlays the first four CTW eigenfunction at 25°S along the coast of Chile and at 11°S along the Angolan coast, following the path where eigenfunctions are orthonormal. For instance, in the SEA at 11°S, in addition to a coastal mooring, bottom pressure measurements at ∼32 km (CTW m2 = 0), ∼105 km (CTW m1∼0) and ∼200 km (statistical offshore mode) offshore would allow disentangling the contribution of the remotely forced second CTW mode from the wind-forced first CTW mode, with CTW modes 3 and 4 having small contribution (cf., companion paper, Illig et al., 2018). As the stratification and the cross-shore bathymetry shape the CTW vertical structures (section 5.1), such diagnostics can help design a coastal observation network for the monitoring of the passage of CTW at key latitudes along the coast.

The overall good agreement between ROMS and LCM coastal SSLA along the coast of southwestern South American and African continents highlights the importance of the CTW dynamics which controls a substantial part of the subseasonal coastal variability. We believe that the ability of the linear model to reproduce the coastal subseasonal variability is encouraging for the understanding of the low-frequency coastal variability in both systems. In the companion paper (Illig et al., 2018), we will benefit from the ROMS and LCM estimations of the dominant CTW mode amplitudes to investigate the similarities and the differences between the two basins regarding the connection with equatorial variability as observed from altimetry. In particular, the experimentation with ROMS and LCM models will allow disentangling the signature of CTW propagations triggered by local wind-stress fluctuations on the coastal variability from that associated with the oceanic remote equatorial forcing.

Appendix A: Inferring CTW Mode Amplitude With the Inversion Methodology ROMS^{INV}

In this section, we recall the equations and provide details on our implementation of the inversion methodology (ROMS^{INV}), originally developed by Church et al. (1986a) to infer the amplitude of the gravest CTW modes from in situ observations.

The general principle of ROMS^{INV} extraction technique is built on the hypothesis that along a cross-shore section, the observed variability is explained only by the sum of the gravest CTW modes and possibly additional statistical offshore modes. In this study, ROMS model outputs provide "virtual" measurements of pressure and alongshore current at the model grid points. We use the four gravest CTW modes, whose pressure (alongshore current) spatial structures which depend on the distance from the coast and the depth, are estimated in section 5.1 and noted F_1, F_2, F_3, and F_4 (G_1, G_2, G_3, and G_4). We also use two statistical modes, labeled $S_P(x,z)$ and $S_V(x,z)$, which are the statistical pressure and alongshore currents offshore modes, respectively. Following Freeland et al. (1986) and Church et al. (1986a), $S_P(x,z)$ ($S_V(x,z)$) is defined as the linear regression coefficient between ROMS offshore subseasonal pressure (alongshore current) time series at $z=1,000$ m and the subseasonal pressure (alongshore current) time series at all locations within the cross-shore section.

It follows that, at each cross-shore section, the amplitude the CTW modes should be a solution of the following equation system, with a minimum residual:

$$\boldsymbol{U}=\boldsymbol{MY} \tag{A1}$$

where:

* **U** is a vector listing N available pressure ($p(x,z)$) measurements and M available alongshore current ($v(x',z')$) observations along a cross-shore section, such as:

$$\boldsymbol{U}=\begin{bmatrix} p(x_1,z_1) \\ \vdots \\ p(x_N,z_N) \\ v(x'_1,z'_1) \\ \vdots \\ v(x'_M,z'_M) \end{bmatrix}$$

* **M** is a matrix containing the structure of the gravest CTW modes and the offshore statistical modes at the location of the measurement points. **M** writes:

$$\boldsymbol{M}=\begin{bmatrix} F_1(x_1,z_1) & F_2(x_1,z_1) & F_3(x_1,z_1) & F_4(x_1,z_1) & S_P(x_1,z_1) & 0 \\ \vdots & \vdots & \vdots & \vdots & \vdots & \vdots \\ F_1(x_N,z_N) & F_2(x_N,z_N) & F_3(x_N,z_N) & F_4(x_N,z_N) & S_P(x_N,z_N) & 0 \\ G_1(x'_1,z'_1) & G_2(x'_1,z'_1) & G_3(x'_1,z'_1) & G_4(x'_1,z'_1) & 0 & S_V(x'_1,z'_1) \\ \vdots & \vdots & \vdots & \vdots & \vdots & \vdots \\ G_1(x'_M,z'_M) & G_2(x'_M,z'_M) & G_3(x'_M,z'_M) & G_4(x'_M,z'_M) & 0 & S_V(x'_M,z'_M) \end{bmatrix}$$

* **Y** is the unknown of the system, i.e., the amplitudes ϕ of each CTW and statistical modes, such as:

$$\boldsymbol{Y}=\begin{bmatrix} \phi_1 \\ \phi_2 \\ \phi_3 \\ \phi_4 \\ \phi_P \\ \phi_V \end{bmatrix}$$

Equation (A1) is solved by least squares fit. The term ***Y*** is the Moore Penrose solution:

$$\boldsymbol{Y}=\left[\left(\boldsymbol{M}^T\boldsymbol{M}\right)^{-1}\boldsymbol{M}^T\right]\ \boldsymbol{U} \tag{A2}$$

solved using singular value decomposition (see Church et al., 1986a for more details), using an effective rank $R=5$. Note that in order to give the same weight to the pressure and alongshore current equations, CTW and statistical modes in ***M*** are normalized by their spatial standard deviation. Then, each element of $\left[\left(\boldsymbol{M}^T\boldsymbol{M}\right)^{-1}\boldsymbol{M}^T\right]$ is multiplied by the associated norm before calculating ***Y*** in equation (A2).

Since the depth of ROMS sigma levels varies in time due to SLA fluctuations (Song & Haidvogel, 1994), at each grid point, ROMS pressure and alongshore current fields are interpolated to their minimum depth encountered over the 2000–2008 period. This allows to compute subseasonal anomalies on time-fixed vertical levels, as well as to accurately estimate the pressure and alongshore statistical modes. Note that, this costly step is mandatory for the inversion methodology, but not for the projection methodology, for which subseasonal anomalies can be calculated after the projection of pressure field onto CTW modal structures (equation (5)). Notably, CTW structures are estimated over a finer grid (2 km-100 regularly spaced sigma vertical level grid) than ROMS grid (1/12°–37 sigma vertical levels stretched in the surface layer). To apply ROMS^{INV}, we linearly interpolate CTW modal structures onto ROMS grid and proceed to the modal decomposition using ROMS pressure and alongshore current outputs at the model grid points.

Limitations of this method are discussed in sections 4.2.1 and 6.

References

Bachèlery, M.-L. (2016). *Variabilité côtière physique et biogéochimique en Atlantique Sud-Est: rôle du forçage atmosphérique local versure téléconnexion océanique* (PhD thesis, 215 pp.). Toulouse, France: Laboratoire d'Etude en Geophysique et Océanographie Spatiale (LEGOS), University of Paul Sabatier.

Bachèlery, M.-L., Illig, S., & Dadou, I. (2016a). Interannual variability in the South-East Atlantic Ocean, focusing on the Benguela Upwelling System: Remote versus local forcing. *Journal of Geophysical Research: Oceans*, *120*, 284–310. https://doi.org/10.1002/2015JC011168

Bachèlery, M.-L., Illig, S., & Dadou, I. (2016b). Forcings of nutrient, oxygen and primary production interannual variability in the South-East Atlantic Ocean. *Geophysical Research Letters*, *43*, 8617–8625. https://doi.org/10.1002/2016GL070288

Bakun, A., & Weeks, S. J. (2008). The marine ecosystem off Peru: What are the secrets of its fishery productivity and what might its future hold? *Progress in Oceanography*, *79*, 290–299.

Belmadani, A., Echevin, V., Dewitte, B., & Colas, F. (2012). Equatorially forced intraseasonal propagations along the Peru-Chile coast and their relation with the nearshore eddy activity in 1992–2000: A modeling study. *Journal of Geophysical Research*, *117*, C04025. https://doi.org/10.1029/2011JC007848

Acknowledgements

We would like to thank the CNES (OSTST project EBUS-SOUTH) for financial support. Marie-Lou Bachèlery received funding from the EU FP7/2007–2013 under grant agreement 603521 and the NRF SARCHI chair on modeling ocean atmosphere land interactions. Marion Kersalé acknowledges support from a NRF grant via a South-African postdoctoral fellowship. Marion Kersalé's work on this study was carried out in part under the auspices of the Cooperative Institute for Marine and Atmospheric Studies (CIMAS), a Cooperative Institute of the University of Miami and the National Oceanic and Atmospheric Administration (NOAA), cooperative agreement NA10OAR4320143. Marion Kersalé also acknowledges support from the NOAA Atlantic Oceanographic and Meteorological Laboratory. The authors would like to thank Boris Dewitte for helpful suggestions throughout the course of this study and in particular some of the early discussions regarding Figure 12. We sincerely acknowledge our native (English) scientist Ross Blamey, who kindly helped us improve the writing of the manuscript. We are also grateful to Kenneth H. Brink and Stephen Van Gorder for sharing their programs and kindly answered some technical questions. Special thanks are addressed to Pauline Charyuer for participating in the sensitivity tests at an early stage of this work. Computations were performed using facilities provided by the University of Cape Town's ICTS High-Performance Computing team (http://hpc.uct.ac.za). The ROMS model grid, forcing, and initial conditions were built using the ROMS_TOOLS package (Penven et al., 2008) version 3.1. The authors wish to acknowledge use of the Ferret program (NOAA PMEL, http://ferret.pmel.noaa.gov) for analysis and graphics in this paper. Gibbs-SeaWater Oceanographic Toolbox and Brink and Chapman (1987) programs are freely available at http://www.teos-10.org/software.htm and http://www.whoi.edu/cms/files/Fortran_30425.htm, respectively. ROMS model and ROMS_TOOLS software can be downloaded from https://www.croco-ocean.org. QuikSCAT wind stress data, AVISO Altimetric data, SODA and ERA-INTERIM reanalysis outputs are freely available to the public on the dedicated websites of these programs. We thank the anonymous reviewers for their comments and suggestions that helped improved the manuscripts.

Blanke, B., Speich, S., Bentamy, A., Roy, C., & Sow, B. (2005). Modeling the structure and variability of the southern Benguela upwelling using QuikSCAT wind forcing. *Journal of Geophysical Research*, *110*, C07018. https://doi.org/10.1029/2004JC002529

Boyer, T. P., Antonov, J. I., Baranova, O. K., Garcia, H. E., Johnson, D. R., Locarnini, R.A., et al. (2009). World ocean database 2009, 1, Introduction. In S. Levitus (Ed.), *NOAA Atlas NESDIS* (Vol. 66). Silver Spring, MD: NOAA.

Brink, K. H. (1982). A comparison of long coastal trapped wave theory with observations off Peru. *Journal of Physical Oceanography*, *12*, 897–913.

Brink, K. H. (1989). Energy conservation in coastal-trapped wave calculations. *Journal of Physical Oceanography*, *19*, 1011–1016.

Brink, K. H. (1991). Coastal-trapped waves and wind-driven currents over the continental shelf. *Annual Review of Fluid Mechanics*, *23*, 389–412. https://doi.org/10.1146/annurev.fl.23.010191.002133

Brink, K. H., Allen, J. S., & Smith, R. L. (1978). A study of low-frequency fluctuations near the Peru coast. *Journal of Physical Oceanography*, *8*, 1025–1041. https://doi.org/10.1175/1520-0485(1978)008<1025:ASOLFF>2.0.CO;2

Brink, K. H., & Chapman, D. C. (1987). *Programs for computing properties of coastal-trapped waves and wind-driven motions over the continental shelf and slope* (Tech. Rep. WHOI-87-24, 122 pp). Woods Hole, MA: Woods Hole Institution.

Cane, M. A., & Sarachik, E. S. (1979). Forced baroclinic ocean motions. III: The linear equatorial basin case. *Journal of Marine Research*, *37*, 355–398.

Carton, J. A., Chepurin, G., & Cao, X. (2000). A simple ocean data assimilation analysis of the global upper ocean 1950–95. Part I: Methodology. *Journal of Physical Oceanography*, *30*, 294–309.

Carton, J. A., & Giese, B. S. (2008). A reanalysis of ocean climate using simple ocean data assimilation (SODA). *Monthly Weather Review*, *136*, 2999–3017. https://doi.org/10.1175/2007MWR1978.1

Carton, J. A., Giese, B. S., & Grodsky, S. A. (2005). Sea level rise and the warming of the oceans in the SODA ocean reanalysis. *Journal of Geophysical Research*, *110*, C09006. https://doi.org/10.1029/2004JC002817

Chapman, D. C. (1985). Numerical treatment of cross-shelf open boundaries in a barotropic coastal ocean model. *Journal of Physical Oceanography*, *15*, 1060–1075.

Chapman, D. C. (1987). Application of wind-forced, long, coastal-trapped wave theory along the California coast. *Journal of Geophysical Research*, *92*, 1789–1816.

Chavez, F., Bertrand, A., Guevara-Carrasco, R., Soler, P., & Csirke, J. (2008). The northern Humboldt current system: Brief history, present status and a view towards the future. *Progress in Oceanography*, *79*, 95–105.

Church, J. A., Freeland, H. J., & Smith, R. L. (1986a). Coastal-trapped waves on the east Australian continental shelf. Part I: Propagation of modes. *Journal of Physical Oceanography*, *16*, 1929–1943.

Church, J. A., White, N. J., Clarke, A. J., Freeland, H. J., & Smith, R. L. (1986b). Coastal-trapped waves on the east Australian continental shelf. Part II: Model verification. *Journal of Physical Oceanography*, *16*, 1945–1957.

Clarke, A. J. (1977). Observational and numerical evidence for wind-forced coastal trapped long wave. *Journal of Physical Oceanography*, *7*, 231–247.

Clarke, A. J. (1983). The reflection of equatorial waves from oceanic boundaries. *Journal of Physical Oceanography*, *13*, 1193–1207.

Clarke, A. J., & Ahmed, R. (1999). Dynamics of remotely forced intraseasonal oscillations off the western coast of South America. *Journal of Physical Oceanography*, *29*, 240–258.

Clarke, A. J., & Brink, K. H. (1985). The response of stratified, frictional flow of shelf and slope waters to fluctuating large-scale low-frequency wind forcing. *Journal of Physical Oceanography*, *15*, 439–453.

Clarke, A. J., & Van Gorder, S. (1986). A method for estimating wind-driven frictional, time-dependent, stratified shelf and slope water flow. *Journal of Physical Oceanography*, *16*, 1013–1028.

Cornejo-Rodriguez, M. P., & Enfield, D. B. (1987). Propagation and forcing of high-frequency sea level variability along the west coast of South America. *Journal of Geophysical Research*, *92*, 14,323–14,334. https://doi.org/10.1029/JC092iC13p14323

Davis, R. E., & Bogden, P. S. (1989). Variability on the California shelf forced by local and remote winds during the coastal ocean dynamics experiment. *Journal of Geophysical Research*, *94*, 4763–4787.

Debreu, L., Marchesiello, P., Penven, P., & Cambon, G. (2012). Two-way nesting in split-explicit ocean models: Algorithms, implementation and validation. *Ocean Modelling*, *49–50*, 1–21.

Dee, D. P., Uppala, S. M., Simmons, A. J., Berrisford, P., Poli, P., Kobayashi, S., et al. (2011). The ERA-Interim reanalysis: Configuration and performance of the data assimilation system. *Quarterly Journal of Royal Meteorological Society*, *137*, 553– 597. https://doi.org/10.1002/qj.828

Desbiolles, F., Blanke, B., Bentamy, A., & Roy, C. (2016). Response of the Southern Benguela upwelling system to fine-scale modifications of the coastal wind. *Journal of Marine Systems*, *156*, 46–55. pp

Dewitte, B., Purca, S., Illig, S., Renault, L., & Giese, B. (2008a). Low frequency modulation of the intraseasonal equatorial Kelvin wave activity in the Pacific Ocean from SODA: 1958–2001. *Journal of Climate*, *21*, 6060–6069.

Dewitte, B., Ramos, M., Echevin, V., Pizarro, O., & duPenhoat, Y. (2008b). Vertical structure variability in a seasonal simulation of a medium-resolution regional model simulation of the South Eastern Pacific. *Progress in Oceanography*, *79*, 120–137.

Dewitte, B., Vazquez-Cuervo, J., Goubanova, K., Illig, S., Takahashi, K., Cambon, G., et al. (2012). Change in El Niño flavours over 1958–2008: Implications for the long-term trend of the upwelling off Peru. *Deep Sea Research Part II: Topical Studies in Oceanography*, *77–80*, 143–156. https://doi.org/10.1016/j.dsr2.2012.04.011

Ducet, N., Le Traon, P. Y., & Reverdin, G. (2000). Global high-resolution mapping of ocean circulation from TOPEX/Poseidon and ERS-1 and-2. *Journal of Geophysical Research*, *105*, 19477–19498. https://doi.org/10.1029/2000JC900063

Dunn, J. R., & Ridgway, K. R. (2002). Mapping ocean properties in regions of complex topography. *Deep Sea Research Part I: Oceanographic Research Papers*, *49*(3), 591–604. https://doi.org/10.1016/S0967-0637(01)00069-3

Echevin, V., Aurelie, A., Marina, L., Michelle, G., Olivier, A., Alice, P., et al. (2014). Intraseasonal variability of nearshore productivity in the Northern Humboldt Current System: The role of coastal trapped waves. *Continental Shelf Research*, *73*(1), 14–30.

Enfield, D. B., Cornejo-Rodriguez, M. P., Smith, R. L., & Newberger, P. A. (1987). The equatorial source of propagating variability along the Peru coast during the 1982–1983 El Niño. *Journal of Geophysical Research*, *92*, 14335–14346. https://doi.org/10.1029/JC092iC13p14335

Florenchie, P., Reason, C. J. C., Lutjeharms, J. R. E., Rouault, M., Roy, C., & Masson, S. (2004). Evolution of interannual warm and cold events in the southeast Atlantic Ocean. *Journal of Climate*, *17*, 2318–2334. https://doi.org/10.1175/1520-0442(2004)017<2318:EOIWAC>2.0.CO;2

Freeland, H. J., Boland, F. M., Church, J. A., Clarke, A. J., Forbes, A. M. G., Huter, A., et al. (1986). The Australian coastal experiment: A search for coastal-trapped waves. *Journal of Physical Oceanography*, *16*, 1230–1249.

Goubanova, K., Illig, S., Machu, E., Garçon, V., & Dewitte, B. (2013). SST subseasonal variability in the Benguela upwelling system as inferred from satellite observations (2000–2008). *Journal of Geophysical Research: Oceans*, *118*, 4092–4110. https://doi.org/10.1002/jgrc.20287

Gruber, N., Lachkar, Z., Frenzel, H., Marchesiello, P., Münnich, M., McWilliams, J. C., et al. (2011). Eddy-induced reduction of biological production in eastern boundary upwelling systems. *Nature Geoscience*, *4*, 787–792. https://doi.org/10.1038/ngeo1273

Gutknecht, E., Dadou, I., Marchesiello, P., Cambon, G., Le Vu, B., Sudre, J., et al. (2013). Nitrogen transfers off Walvis Bay: A 3-D coupled physical/biogeochemical modeling approach in the Namibian upwelling system. *Biogeosciences*, *10*(6), 4117–4135. https://doi.org/10.5194/bg-10-4117-2013

Hayashi, Y. (1982). Space-time spectral analysis and its applications to atmospheric waves. *Journal of Meteorological Society of Japan*, *60*, 156–171.

Hormazabal, S., Shaffer, G., Letelier, J., & Ulloa, O. (2001). Local and remote forcing of sea surface temperature in the coastal upwelling system off Chile. *Journal of Geophysical Research*, *106*, 16,657–16,671. https://doi.org/10.1029/2001JC900008

Hormazabal, S., Shaffer, G., & Pizarro, O. (2002). Tropical Pacific control of intraseasonal oscillations off Chile by way of oceanic and atmospheric pathways. *Geophysical Research Letters*, *29*(6), 1081. https://doi.org/10.1029/2001GL013481

Huthnance, J. M. (1978). On coastal trapped waves: Analysis and numerical calculation by inverse iteration. *Journal of Physical Oceanography*, *8*, 74–92.

Huthnance, J. M. (1995). Circulation, exchange and water masses at the ocean margin: the role of physical processes at the shelf edge. *Progress in Oceanography*, *35*, 353–431. https://doi.org/10.1016/0079-6611(95)80003-C

Illig, S., Dewitte, B., Ayoub, N., Du Penhoat, Y., Reverdin, G., De Mey, P., et al. (2004). Interannual long equatorial waves in the tropical Atlantic from a high-resolution ocean general circulation model experiment in 1981–2000. *Journal of Geophysical Research*, *109*, C02022. https://doi.org/10.1029/2003JC001771

Illig, S., Dewitte, B., Goubanova, K., Cambon, G., Boucharel, J., Monetti, F., et al. (2014). Forcing mechanisms of intraseasonal SST variability off Central Peru in 2000–2008. *Journal of Geophysical Research: Oceans*, *119*, 3548–3573. https://doi.org/10.1002/2013JC009779

Illig, S., Bachélery, M.-L., & Cadier, E. (2018). Subseasonal coastal-trapped wave propagations in the southeastern Pacific and Atlantic Oceans: 2. Wave characteristics and connection with the equatorial variability. *Journal of Geophysical Research: Oceans*, *123*, 3942–3961. https://doi.org/10.1029/2017JC013540

Johnson, E. R. (1991). The scattering at low frequencies of coastally trapped waves. *Journal of Physical Oceanography*, *21*, 913–932.

Jordi, A., Orfila, A., Basterretxea, G., & Tintoré, J. (2005). Coastal trapped waves in the Northwestern Mediterranean. *Continental Shelf Research*, *25*, 185–196.

Kondo, J. (1975). Air-sea bulk transfer coefficients in diabatic conditions. *Boundary-Layer Meteorology*, *9*, 91–112.

Kopte, R., Brandt, P., Dengler, M., Tchipalanga, P. C. M., Macuéria, M., & Ostrowski, M. (2017). The Angola Current: Flow and hydrographic characteristics as observed at 11°S. *Journal of Geophysical Research: Oceans*, *122*, 1177–1189. https://doi.org/10.1002/2016JC012374

Large, W., McWilliams, J., & Doney, S. (1994). Oceanic vertical mixing: A review and a model with a nonlocal boundary layer parameterization. *Reviews of Geophysics*, *32*, 363–403.

Leth, O. (2000). *Ocean circulation in the eastern South Pacific: An observational and numerical modelling study* (PhD thesis, 184 pp.). Copenhagen, Denmark: Niels Bohr Institute, University of Copenhagen.

Leth, O., & Middleton, J. F. (2004). A mechanism for enhanced upwelling off Central Chile: Eddy advection. *Journal of Geophysical Research*, *109*, C12020. https://doi.org/10.1029/2003JC002129

Le Traon, P. Y., Nadal, F., & Ducet, N. (1998). An improved mapping method of multisatellite altimeter data. *Journal of Atmospheric Oceanic Technology*, *15*(2), 522–534. https://doi.org/10.1175/1520-0426

Marchesiello, P., & Estrade, P. (2010). Upwelling limitation by onshore geostrophic flow. *Journal of Marine Research*, *68*(1), 37–62.

Marchesiello, P., McWilliams, J. C., & Shchepetkin, A. (2001). Open boundary conditions for long-term integration of regional oceanic models. *Ocean Modelling*, *3*, 1–20.

McDougall, T. J., & Barker, P. M. (2011). *Getting started with TEOS-10 and the Gibbs Seawater (GSW) Oceanographic Toolbox* (SCOR/IAPSO WG127, 28pp.).

Mitchum, G. T., & Clarke, A. J. (1986). The frictional nearshore response to forcing by synoptic scale winds. *Journal of Physical Oceanography*, *16*, 934–946.

Moore, D. W. (1968). Planetary-gravity waves in an equatorial ocean (PhD thesis). Cambridge, MA: Harvard University.

Mosquera-Vásquez, K., Dewitte, B., & Illig, S. (2014). The Central Pacific El Niño intraseasonal Kelvin wave. *Journal of Geophysical Research: Oceans*, *119*, 6605–6621. https://doi.org/10.1002/2014JC010044

Penven, P., Debreu, L., Marchesiello, P., & McWilliams, J. C. (2006). Evaluation and application of the ROMS 1-way embedding procedure to the central california upwelling system. *Ocean Modelling*, *12*, 157–187.

Penven, P., Marchesiello, P., Debreu, L., & Lefevre, J. (2008). Software tools for pre- and post-processing of oceanic regional simulations. *Environmental Modelling & Software*, *23*, 660–662.

Pizarro, O., Clarke, A. J., & Van Gorder, S. (2001). El Niño sea level and currents along the South American coast: Comparison of observations with theory. *Journal of Physical Oceanography*, *31*(7), 1891–1903.

Pizarro, O., Shaffer, G., Dewitte, B., & Ramos, M. (2002). Dynamics of seasonal and interannual variability of the Peru–Chile Undercurrent. *Geophysical Research Letters*, *29*(12), 1581.

Polo, I., Lazar, A., Rodriguez-Fonseca, B., & Arnault, S. (2008). Oceanic Kelvin waves and tropical Atlantic intraseasonal variability: 1. Kelvin wave characterization. *Journal of Geophysical Research*, *113*, C07009. https://doi.org/10.1029/2007JC004495

Ridgway, K. R., Dunn, J. R., & Wilkin, J. L. (2002). Ocean interpolation by four-dimensional least squares: Application to the waters around Australia. *Journal of Atmospheric Oceanic Technology*, *19*(9), 1357–1375.

Rouault, M., Illig, S., Bartholomae, C., Reason, C. J. C., & Bentamy, A. (2007). Propagation and origin of warm anomalies in the Angola Benguela upwelling system in 2001. *Journal of Marine Systems*, *68*, 473–488. https://doi.org/10.1016/j.jmarsys.2006.11.010

Rouault, M., Illig, S., Lübbecke, J., & Imbol Koungue, R. A. (2017). Origin, development and demise of the 2010–2011 Benguela Niño. *Journal of Marine Systems*, in press. https://doi.org/10.1016/j.jmarsys.2017.07.007

Schumann, E. H., & Brink, K. H. (1990). Coastal-trapped waves off the coast of South Africa: Generation, Propagation and current structures. *Journal of Physical Oceanography*, *20*, 1206–1218.

Sciremammano, F. (1979). A suggestion for the presentation of correlations and their significance levels. *Journal of Physical Oceanography*, *9*, 1273–1276.

Shaffer, G., Pizarro, O., Djurfeldt, L., Salinas, S., & Rutllant, J. (1997). Circulation and low-frequency variability near the Chilean coast: Remotely forced fluctuations during the 1991–1992 El Niño. *Journal of Physical Oceanography*, *27*, 217–235.

Shchepetkin, A. F., & McWilliams, J. C. (1998). Quasi-monotone advection schemes based on explicit locally adaptive dissipation. *Monthly Weather Review*, *126*, 1541–1580. https://doi.org/10.1175/1520-0493(1998)126<1541:QMASBO>2.0.CO;2

Shchepetkin, A. F., & McWilliams, J. C. (2005). The Regional Oceanic Modeling System: A split-explicit, free-surface, topography following-coordinate ocean model. *Ocean Modelling*, *9*, 347–404. https://doi.org/10.1016/j.ocemod.2004.08.002

Smith, R. L. (1978). Poleward propagating perturbations in currents and sea levels along the Peru coast. *Journal of Geophysical Research*, *83*, 6083–6092. https://doi.org/10.1029/JC083iC12p06083

Song, Y., & Haidvogel, D. B. (1994). A semi-implicit ocean circulation model using a generalized topography-following coordinate system. *Journal Computational Physics*, *115*(1), 228–244.

Stuart, D. W. (1981). Sea-surface temperatures and winds during JOINT II: 2. Temporal fluctuations. In F. A. Richards (Ed.), *Coastal upwelling, coastal estuarine science series* (Vol. 1,pp. 32–38). Washington, DC: AGU.

Taylor, K. E. (2001). Summarizing multiple aspects of model performance in a single diagram. *Journal of Geophysical Research*, *106*, 7183–7192.

Wang, D.-P., & Mooers, C. (1976). Coastal-trapped waves in a continuously stratified ocean. *Journal of Physical Oceanography*, *6*, 853–856.

Yin, L., Qiao, F., & Zheng, Q. (2014). Coastal-trapped waves in the East China Sea observed by a mooring array in winter 2006. *Journal of Physical Oceanography*, *44*(2), 576–590.